African swine fever virus gene B117L encodes for a small protein endowed with low pH-dependent membrane permeabilizing activity

D. P. Gladue[a]*, L. Gomez-Lucas[b], E. Largo[b,c], L. Velazquez-Salinas[a], E. Ramirez-Medina[a], J. Torralba[b], M. Queralt[d], A. Alcaraz[d], J. L. Nieva[b]*, and M. V. Borca[a]*

[a] Plum Island Animal Disease Center, ARS, USDA, Greenport, NY 11944, USA.

[b] Instituto Biofisika (CSIC-UPV/EHU) and Department of Biochemistry and Molecular Biology, University of the Basque Country, P.O. Box 644, 48080 Bilbao, Spain.

[c] Department of Immunology, Microbiology and Parasitology, Faculty of Pharmacy, University of the Basque Country UPV/EHU, 01006 Vitoria-Gasteiz, Spain.

[d] Laboratory of Molecular Biophysics. Department of Physics. University Jaume I, 12071 Castellón, Spain

*Corresponding author:

Mailing address: M. V. Borca / D.P. Gladue
Plum Island Animal Disease Center, USDA/ARS/NAA
P.O. Box 848, Greenport, NY 11944-0848
TEL: (631) 323-3019
FAX: (631) 323-3006
E-mail: manuel.borca@ars.usda.gov / douglas.gladue@usda.gov

J.L. Nieva
Instituto Biofisika (CSIC-UPV/EHU) and Department of Biochemistry and Molecular Biology, University of the Basque Country, P.O. Box 644, 48080 Bilbao, Spain
TEL:+34 94 601 3353
FAX: +34 94 601 3360
E-mail: joseluis.nieva@ehu.eus

Abstract

African swine fever virus (ASFV) is causing a devastating pandemic in domestic and wild swine within Central Europe to East Asia resulting in economic losses for the swine industry. The virus contains a large double-stranded DNA genome that encodes for more than 150 genes, most with no experimentally characterized function. In this study, we evaluate the potential function of ASFV gene B117L, a 115 amino acid integral membrane protein transcribed at late times during the virus replication cycle and showing no homology to any previously published protein. Hydrophobicity distribution along B117L confirmed the presence of a single transmembrane helix, which, in combination with flanking amphipathic sequences, composes a potential membrane-associated C-terminal domain of ca. 50 amino acids. Ectopic transient cell expression of the B117L gene as a GFP fusion protein revealed the co-localization with markers of the Endoplasmic Reticulum (ER). Intracellular localization of various B117L constructs also displayed a pattern for the formation of organized smooth ER (OSER) structures compatible with the presence of a single transmembrane helix with a cytoplasmic carboxy terminus. Using partially overlapping peptides, we further demonstrate that the B117L transmembrane helix has the capacity to establish spores and ion channels in membranes at low pH. Furthermore, our evolutionary analysis showed the high conservation of the transmembrane domain during the evolution of the B117L gene, indicating that the integrity of this domain is preserved by the action of the purifying selection. Collectively our data support a viroporin-like assistant role for the B117L gene-encoded product in ASFV entry.

Importance

ASFV is responsible for an extensively distributed pandemic causing important economic losses in the pork industry in Eurasia. The development of countermeasures is partially limited by the insufficient knowledge regarding the function of the majority of the more than 150 genes encoded by the virus genome. Here we provide data regarding the functional experimental evaluation of a previously uncharacterized ASFV gene, B117L. Our data suggest that the B117L gene encodes for a small membrane protein that assist in the permeabilization of the ER-derived envelope during ASFV infection.

Introduction

African swine fever (ASF) is currently affecting the swine production industry in a large geographical area stretching across Europe and into East and Southeast Asia. In July 2021, the Dominican Republic reported its first outbreak of ASF, which had been absent from North America for 40 years. As a result, global swine industries are threatened by significant economic losses and human populations face food insecurity (1). Disease control is currently restricted to culling susceptible animals and implementing strict biosecurity measures to prevent disease spread since no commercial vaccines are available.

The etiological agent, African swine fever virus (ASFV), is a large, structurally complex virus with a large (more than 180 kb pairs) double-stranded DNA genome (2). ASFV encodes for more than 150 genes, most of which remain uncharacterized (1, 2). Understanding the function of virus genes is critical for the development of experimental vaccines and novel countermeasures (3-9).

Here, we study the role of the structural B117L gene which is predicted to encode a short integral membrane protein (IMP) (10) comprised in the proteome of the ASFV (11) but not having a known function. 3D-structure prediction and hydrophobicity distribution along its sequence, reveal the presence of an N-terminal small globular ectodomain that is followed by an "amphipathic-strand/hydrophobic-helix/amphipathic-helix" membrane domain (MD) roughly spanning 50 amino acids.

Moreover, the B117L structural gene is transcribed late in the replicative cell cycle of the virus consistent with functional roles of the encoded protein during entry. The protein B117L, when expressed in cells in the absence of a signal sequence, localized in the ER membrane adopting a topology that appeared dictated by the transmembrane helix (TMH) moiety. In addition, synthetic peptides representing the MD sequence demonstrated the potential of the protein encoded by B117L gene to interact with membranes, along with a membrane-permeabilizing and ion-channel activities for the amino acid stretch spanning the TMH, particularly at low pH. Therefore, our data seem to indicate that the B117L gene encodes for a protein that could embody a structural viroporin, whose activity is triggered at the low pH of the endosome during cell entry.

Materials and Methods

Phylogenetic analysis

To determine the genetic relationship among ASFV isolates representing the genetic diversity of B117L gene in nature, a phylogenetic analysis was conducted using the maximum likelihood method and the Tamura 3-parameter model (12). The use of this model was supported based on the Bayesian Information Criterion (BIC) score (1762.273). The reliability of the phylogenetic topology was tested using 1000 bootstrap

replications. The nucleotide alignment used for this analysis was obtained by the algorithm MUSCLE codons (multiple sequence comparison by log-expectation) (13) and the analysis was carried out using the software Mega version 10.2.5 (14).

The number of nucleotide and amino acid differences per site (pairwise distance calculations) at B117L gene among representative ASFV field isolates were calculated by pairwise distance analyses using the p-distance model. To determine the standard error, 1000 bootstraps replicates were used. Analysis was carried out using the software Mega version 10.2.5 (14).

Evolutionary analysis

To infer the evolutionary dynamics of B117L gene in nature, we used a systematic approach previously published in ASFV (15, 16, 17) and SARS-CoV-2 (18). This approach considers the different modes by which natural selection can be manifested (diversifying: including episodic and pervasive selection, or purifying), and is associated to the combination of multiple maximum likelihood evolutionary algorithms that infer rates of synonymous (dS) and nonsynonymous substitutions on a per site basis in a codon base phylogenetic framework (19). In this context, to identify relevant sites on B117L gene experiencing diversifying (positive selection) and purifying (negative selection) we used the Single Likelihood Ancestor Counting (SLAC), the Fixed Effects Likelihood (FEL) (20), and the Mixed Effects Model of Evolution (MEME) (21) algorithms. MEME is the only algorithm specialized in the detection of both pervasive and episodic diversifying selection, so that higher detection rates are expected using this algorithm (22).

The potential role of positive selection in the evolution of specific phenotypes of B117L gene in nature was identified by using a combination of two specific algorithms specialized in detection of episodic diversifying selection at specific branches of the phylogenetic tree: aBSREL (adaptive Branch Site Random Effects Likelihood) (23) and BUSTED (Branch-Site Unrestricted Statistical Test for Episodic Diversification). aBSREL was used as exploratory analysis to test all branches in the phylogeny for the detection of specific branches under positive selection (it uses the likelihood ratio test statistic for the selection, LRT, of relevant branches and the Holm-Bonferroni method for the correction p-values). BUSTED (used here to support the results obtained by aBSREL) is an algorithm used to detect gene-wide positive selection, testing the hypothesis whether a gene has experienced positive selection in at least one of the sites in the branches by contrasting the values obtained by the unconstrained model (alternative model of positive selection) with the ones calculated for the constrained model (null model disallowing positive selection). The existence of positive selection was supported by the likelihood ratio test statistic for the selection (24).

The existence of recombination during the evolution of B117L gene was assessed by the algorithm GARD (Genetic Algorithm for Recombination Detection) (25). GARD evaluates a multiple sequencing-alignment for the presence of putative recombination breakpoints, quantifying the level of support for their locations, and identifying topology incongruences in the phylogeny that may evidence potential recombination events. GARD verifies the incongruence between adjacent partitions using posteriori incongruence tests (SH test).

Detection of B117L Transcription

As previously described (26), we used a real-time PCR assay (qPCR) to evaluate the transcriptional profile of the B117L gene during the infection of ASFV-G in cultures of porcine macrophages, using the early CP204L (p30) and late B646L (p72) expressed genes of ASFV as reference genes. Briefly, cell cultures of porcine macrophages were infected with a stock of ASFV-G using an MOI of 10. RNA extractions using a RNeasy Kit (QIAGEN, Hilden, Germany) were conducted at 4, 6, 8, and 24 h post-infection. All extractions were treated with 2 units of DNase I (BioLabs, San Diego, CA, USA) then purified using the Monarch® RNA Cleanup Kit (New England BioLabs, Inc., Ipswich, MA, USA). One ug of RNA was used to produce cDNA using qScript cDNA SuperMix (Quanta bio, Beverly, MA, USA) that was used for the qPCR.

Primers and probes for the detection of the B117L gene were designed using the ASFV Georgia 2007/1 strain (GenBank Accession #NC_044959.2). Primer forward: 50- for the detection of p72 gene: forward 50- ACATCTTATGCGACCACATCC-30, reverse:
50- AAATGACTATTAAAATAAAGCCCAAACC-30 and probe: 50-FAM CCACACC TCATGCAGCGGC-MGB NFQ-30. Primers and probes for the detection of CP204L (p30) gene: forward 50-GACGGAATCCTCAGCATCTTC-30, reverse: 50-CAGCTTGGAGT CTTT AGGTACC-30 and probe: 50-FAM-TGTTTGAGCAAGAGCCCTCATCGG-MGB NFQ-30. Primers and probes for the detection of the β-actin gene: forward 50-GACCTGACCGACTACCTCATG-30, reverse: 50-TCTCCTTGATGTCCCGCAC-30 and probe: 50-FAM-CTACAGCTTCACCACCACGGCMGB NFQ-30. All qPCRs were conducted using the TaqMan Universal PCR Master Mix (Applied Biosystems,Waltham, MA, USA) using the

following amplification conditions: One step at 55 ^{o}C for 2 min, followed by one denaturation step at 95 ^{o}C for 10 min, then 40 cycles of denaturation at 95 ^{o}C for 15 s and annealing/extension at 65 ^{o}C for 1 min.

Synthetic peptides, lipids and fluorescent probes

Peptides overlapping the B117L MD sequence were produced by solid synthesis as previously described (27, 28). Synthetic purified peptides were dissolved in dimethyl sulfoxide (DMSO, spectroscopy grade) and their concentrations determined by the bicinchoninic-acid microassay (Pierce, Rockford, IL, USA). Aliquots (typically 20 µL, 1 mg/mL) were stored frozen and were thawed only once, upon use. Phosphatidylcholine (PC), phospahtidylethanolamine (PE), and phosphatidylinositol (PI) were purchased from Avanti Polar Lipids (Birmingham, AL, USA).

Cell expression

Subcellular localization of the expressed B117L protein (ASFV isolate Georgia 2010) and its derived constructs, was assayed by co-transfecting HEK293T or HeLa cells (2×10^5 cells) with plasmids encoding GFP fusions and cell organelle markers (1 µg each, if not stated otherwise) using calcium phosphate (29). Plasmids encoding for the organelle markers were obtained from Addgene (Watertown, MA) and included different proteins and peptides fused to mCherry, namely: cytochrome c oxidase subunit 8A (mitochondria, Plasmid #55102), N-terminal 20 residues of neuromodulin (plasma membrane, Plasmid #55779), BiP (ER soluble, Plasmid #62233) and Sec61β (ER membrane, Plasmid #49155). For constructing the chimera B117L-Sec61TMH-GFP, the nucleotide sequence encoding for B117L amino acids ^{69}IFNGLGFILIVIFIYLLLITLQQMLTRHI^{97} was

substituted by that encoding the Sec61γ sequence: FQKIAMATAIGFAIMGFIGFFVKLIHIPI (30).

At 36 h post-transfection, cells were observed under the microscope in phosphate saline buffer (PBS). Confocal images were acquired on a Leica TCS SP5 II microscope (Leica Microsystems GmbH, Wetzlar, Germany), using a x63 water-immersion objective, or in a Zeiss LSM800 (Carl-Zeiss-Stiftung, Jena, Germany) using a Plan Apochromat x63 oil-immersion objective. Pearson coefficients were calculated using the ImageJ plug-in Coloc 2 (http://imagej.net/Coloc_2) to establish the correlation between fluorescence intensities emitted by green and red flourophores in each pixel of the confocal images.

Oligomerization state was assayed in HEK293 T cells (1.5×10^6 cells) transfected with 10 μg of plasmid encoding GFP or GFP-B117L constructs. Cells were collected in cold PBS at 36 h post-transfection, sonicated for 1 min with a probe tip sonicator (MSE Soniprep 150, MSE, UK) on ice, and finally dissolved in SDS-PAGE loading buffer. Anti-GFP antibody was used to detect oligomers by immunoblot analysis after electrophoresis.

Membrane permeability of single vesicles

For the single vesicle permeability measurements, Giant Unilamellar Vesicles (GUVs) made of PC:PE:PI:Rho-PE (50:30:20:0.1 mole ratio) were prepared and analyzed through quantitative microscopy following protocols described in previous works (31, 32). In brief, 2 μl of the ER lipid mixture (2 mM) were placed on the platinum wires and the solvent evaporated. For GUV electroformation, 2.4 V, 10 Hz were applied during 2 h in a sucrose (300 mM) solution. To promote detachment of the GUVs from the wires 2 Hz were finally applied during 30 min. For confocal microscopy analyses 80 μl of the solution were transferred to 320 μl of buffer (HEPES 10 mM, KCl 150 mM, pH 7.4) in a

Lab-Tek® eight-chambered #1.0 borosilicate cover glass from Nalge Nunc International (Rochester, NY, USA) previously blocked with 2mg/ml BSA.

Confocal fluorescence microscopy images of individual GUVs were obtained using a Leica TCS SP5 II fluorescence microscope (Leica Microsystems GmbH, Wetzlar, Germany). Extents of permeabilization were calculated for each vesicle after 2 hours of incubation with Alexa Fluor 488 and B117L peptides. For this purpose, the fluorescence intensity value outside the vesicle is considered as 100 %, whereas intensity inside vesicles reflected the percentage of probe entry into the vesicle lumen. Fluorescence emission in the different regions of the sample was quantitated after image processing and analyses carried out with ImageJ software (rsb.info.nih.gov/ij/).

Infrared Spectroscopy

Infrared spectra were recorded in a Thermo Nicolet Nexus 5700 (Thermo Fisher Scientific,Waltham, MA) spectrometer equipped with a mercury-cadmium-telluride detector using a Peltier based temperature controller (TempCon, BioTools Inc., Wauconda, IL) with calcium fluoride cells (BioCell, BioTools Inc., Wauconda, IL). Peptide-containing samples (peptide-to-lipid ratio, 1:50) were lyophilized and subsequently prepared at 3 mg (peptide)/mL in D_2O buffer (PBS). A 25 µl sample aliquot was deposited on a cell that was sealed with a second cell. Reference windows without peptide were prepared similarly. Typically 370 scans were collected for each background and sample, and the spectra were obtained with a nominal resolution of 2 cm^{-1}. To obtain the amide I spectra, solvent and membrane contributions were subtracted from the original spectra. Data treatment and band decomposition of the original amide I have been described elsewhere (33).

Ion Channel activity

To form planar membranes, two monolayers (20 µl of lipid mixture at 5 mg/ml in pentane added on 1.8 ml salt solutions) were assembled at both sides of a Teflon chamber partitioned by a 15 µm thick Teflon film with a 120-140 µm diameter orifice, as described previously (34). Monolayer apposition on the orifice (previously treated with a 3% solution of hexadecane in pentane) led to the formation of lipid bilayers (detected by capacitance measurements). B117L peptides dissolved in DMSO were supplemented to the lipid solutions in both sides of the chamber. Conductance measurements were carried out applying an electric potential using Ag/AgCl electrodes in 2 M KCl, 1.5% agarose bridges assembled within standard 250 µl pipette tips. Potential is defined as positive when it is higher at the side closer to the researcher (the cis side), while the trans side is set to ground. The current and applying potential were measured using an Axopatch 200B amplifier (Molecular Devices, Sunnyvale, CA) in the voltage-clamp mode. Current was filtered with a 10 kHz 8-pole in-line Bessel filter and digitized with a Digidata 1440A (Molecular Devices, Sunnyvale, CA) at 50 kHz sampling frequency. The membrane chamber and the head stage were isolated from external noise sources with a double metal screen (Amuneal Manufacturing Corp., Philadelphia, PA). The conductance was obtained from current measurements under an applied potential of 50 mV in symmetrical salt solutions of 150 mM KCl buffered with 5 mM KOAc. Current values were evaluated using the Gaussian fit tool of Clampfit 10.7 (Molecular Devices, Sunnyvale, CA). For each sample, at least 40 different traces were typically recorded (recording time for each trace was 180 s).

Results

Definition of a membrane domain on the ASFV B117L protein

The ASFV B117L gene was predicted to encode an integral membrane protein by Yañez et al. (10), its translated product recently identified through proteomic analysis as a minor structural component of the virion (11). However, the structural organization and possible functions of this ASFV protein remain to be elucidated. After an analysis using the software Pfam 35.0 (35), no significant similarities were found between B117L and a total of 19,632 protein families, indicating the lack of tools to predict functionality based on homologies with annotated sequences.

Topology prediction using the state-of-the-art DeepTMHMM program, which is based on non-homology methods (36), supported the ASFV (isolate Georgia) B117L protein as an alpha helical transmembrane protein without a signal peptide (SP) (Fig. 1A, left panels). This analysis also predicted an N_{out}/C_{in} topology for B117L inserted into cell membranes. Consistently with these data, the 3D-structure prediction by AlphaFold (37) rendered a single helix structure (residues 67-114) including the TMH moiety. Upon insertion of the TMH traversing a POPC bilayer (Fig. 1A, right panel), this long helix was preceded at the N-terminus by a solvent-exposed small globular ectodomain, which contained a defined, shorter helix. Interestingly, the membrane-spanning helix extended into the cytosol exposing to solvent its C-terminal stretch (residues 90-114). Thus, in the absence of additional interactions, this helical stretch would likely unwind due to the competing H-bonds established by the hydrophilic amide backbone with water. In addition, the strand that precedes the predicted TMH at its N-terminus appears to run in contact with the membrane interface at the external side.

To infer alternative arrangements that might contribute to the stability of B117L in contact with membranes, we next determined the hydrophobicity distribution along the sequence based on the Kyte-Doolitle hydropathy scale (38) (Fig. 1B, left). Besides the delineation of the TMH as a prominent positive peak in mean hydrophobicity plots, the analysis of the hydrophobic moments revealed two additional elements with capacity for inserting into membranes, namely: (i) an amphipathic strand at the N-terminal side of the TMH; and (ii) an amphipatic helix at its C-terminus. In conjunction, this 'amphipatic-strand/hydrophobic-helix/amphipatic-helix' motif composes a membrane-associated domain (MD) spanning the sequence 60-109 (i.e., ca. 50 amino acids) of B117L. The structural model displayed in the Figure 1B (left panel) incorporates these MD elements and suggests that a complex pattern of membrane interactions contribute to B117L stability, including the insertion of the C-terminal amphipathic helix into the membrane monolayer facing the cytosol. To allow this process, the new model introduces a kink at the position Arg95-His96, two residues showing strong propensity to locate at turns in transmembrane helices (39).

Genetic diversity of B177L in nature

To evaluate the relevance of the potential ectodomain-MD structural arrangement, we analyzed the genetic diversity of B117L gene of ASFV in nature. We used the Basic Local Alignment Search Tool (BLAST) to perform an exhaustive search of different forms of B117L using as a query the ASFV isolate Georgia (NC_044959.2). As a result of this analysis, a total of eight ASFV isolates were identified as a representative of the genetic diversity of B117L in nature. These isolates included the ASFV genetic groups I, II, IV, VII, VIII, IX and XX (Fig. 2). Overall, pairwise distance analysis depicted average

levels of identity among isolates between 99.71%-79.43% (~91.06%) and 99.14%-82.27% (~91.57%) at nucleotide and amino acid levels respectively, indicating the high level of conservation of B117L among isolates. No differences were predicted among isolates belonging to the pandemic Eurasian lineage (genotype II), indicating that B117L gene is not promoting the diversification of this lineage.

The amino acid alignment showed the different phenotypes associated with B117L gene (Fig. 2A). Several deletions were found within the ectodomain, between amino acids 36 and 50, spanning the loop that connects the α-helix with the amphipathic MD strand, indicating the existence of protein phenotypes of variable lengths. However, a high amino acid conservation was observed in the predicted MD between amino acids 65 and 114, indicating the conservation of this domain during the evolution of B117L gene (note that the numbering used in these analyses corresponds to the Malawi isolate sequence, i.e., longer than that of the Georgia isolate by 5 aa-s).

Based on a phylogenetic analysis using full-length nucleotide sequences of B117L gene (~366 nt), it was possible to classify multiple virus isolates in four different phylogenetic groups (Fig. 2B). Interestingly, as published in our previous studies (15), the phylogenetic relationship among isolates using B117L from different genotypes contrasts with the relationships predicted by the reference p72 gene indicating the complex evolutionary dynamics among different ASFV genes, suggesting that one single gene may not be used to reflect the relationship among ASFV isolates (40).

Effect of natural selection at specific codon sites in B117L gene

To get more insights about the evolutionary dynamics of B117L gene in nature, we evaluated this gene for the presence of specific codon sites evolving under negative or

positive selection. Overall, using the SLAC algorithm, we predicted global rates of dN/dS =0.395, indicating that purifying selection is the main force driving the evolution of B117L gene. Consistently with this result, using the algorithm FEL, we identified a total of 11 codons under purifying selection (Fig. 3A). In this context, these results suggest that ectodomain residues 18, 20, 22, 35, 52, 63 as well as the residues included in the MD (74, 84, 103 and 104) represent residues highly preserved during the evolution of the B117L protein, indicating their potential relevance in its function (Fig. 3B). In case of sites experimenting diversifying selection, the algorithm MEME identifies codons 58 and 59 as relevant ones (Fig. 3A and 3B). Based on the lack of identification of sites under positive selection by FEL, it can be concluded that the selection of ectodomain amino acids 58 and 59 are the resultant of episodic diversifying selection.

Positioning in the predicted structure suggests diverse structural roles for most of these B117L residues (Fig. 3C). Thus, conserved residues Asp18, Thr20 and His22 appear to establish a structurally defined connection at the N-terminus of the α-helix contained within the globular ectodomain, whereas Ala35 marks the end of this element in several isolates (Fig. 2A). In contrast, His58 and Thr59, residues subject to diversifying selection, locate at a mid-point within the following loop. Conserved Pro52 and Pro63 change the backbone direction, the latter to allow the amphipatic strand that precedes the TMH run in contact with the bilayer interface. Similarly, polar Asn104 might serve to stabilize a membrane-associated helix-kink connecting the TMH with the C-terminal amphipatic helix in our model (39). Structural roles requiring conservation beyond retaining a hydrophobic or aromatic character are more difficult to infer for the MD residues Ile74, Val84 or Tyr103. Hence, negative selection applied to

aliphatic/aromatic residues within the MD might reflect functional roles performed by this domain.

Supporting this notion, a pairwise analysis comparing the full-length B117L gene versus the region associated with the MD, it was found that the pairwise distance among isolates was significantly reduced in comparison with the rest of the genome (Fig. 3D), indicating the high conservation of this genome section among ASFV isolates. Furthermore, when the inferred synonymous (dS) and nonsynonymous (dN) substitution rates compared, it is found that synonymous mutations are significantly being fixed 1.84 times faster that nonsynonymous ones (Fig. 3E).

Detection of specific B117L phenotypes evolving as result of positive selection

Based on the results of the phylogenetic analysis presented in Fig. 2B, we decided to include the use of evolutionary algorithms focused on the detection of positive selection at branch level as a concept to detect phenotypes of B117L protein evolving because of positive selection. First, as screening in the phylogeny, all branches were evaluated by the algorithm aBSREL. The results indicated that among multiple branches in the tree, the branch associated with the isolate Ken05/Tk1 was significantly different from the rest of the branches, suggesting that the B117L phenotype of this isolate was the resultant of positive selection (Fig. 4A). To test this hypothesis, we conducted the evolutionary algorithm BUSTED. In this context, the overall dN/dS values in the branch associated with the isolate Ken05/Tk1 (test), were compared with the overall dN/dS values from the rest of the branches in the tree (background). The results of this analysis confirmed the previous inference obtained by aBSREL (LRT, p-value =0.009 $\leq$ .05), indicating that B117L gene present in the Isolate Ken05/Tk1 may represent a

significantly different phenotype in comparison with the rest of the isolates included in this study, and so that highlighting the role of natural selection in the evolution of this phenotype. Furthermore, BUSTED analysis identified amino acids 31, 32, 33, and 34, belonging to the ectodomain α-helix in the rest of the isolates, as potential sites associated with the phenotype difference inferred for B117L gene present in the isolate Ken05/Tk1 (Figs. 4B, and 4C). Supporting the relevance of the helix present in the ectodomain, the prediction of the 3D-structure of the Ken05/Tk1 B117L protein revealed that residues 31-34 could serve to cap a cognate structure at its C-terminus, which, although distorted, is also preserved in this isolate. Interestingly, despite the evidence regarding the potential phenotypic differences in the B117L gene present in Ken05/Tk1, no relevant sites were predicted along MD of this protein, further reinforcing the importance of this domain in performing a common function by ASFV B117L proteins (Fig. 4B).

To test the potential role of recombination during the evolution of B117L gene, sequences of representative ASFV isolates were evaluated by the GARD algorithm. Overall, the results indicated the existence of two potential break points at nucleotides 87 and 170. This inference was supported by an improvement in the AIC-c =1678.90 vs c-AIC= 1650.65 scores, when compared between the model predicting a single partition (no breakpoints) and the model predicting multiple breakpoints respectively. In this context, evident topology incongruences among different gene segments were observed (Fig. 5), suggesting that recombination may be playing a role in the evolution of B117L gene. Interestingly, the absence of potential breakpoints at MD suggests again the preservation of this domain during the evolution of this gene.

B117L gene is transcribed as a late gene

To determine when the B117L gene is transcribed during the replication cycle, a time course experiment was performed to analyze the kinetics of RNA transcription in primary swine macrophages infected with the ASFV strain Georgia. Swine macrophage cultures were infected at a MOI = 1 with ASFV-G, and cell lysate samples were taken at 0, 4, 6, 8, and 24 hpi. The presence of B117L RNA was detected by two-step RT-PCR as described in the Material and Methods Section. Transcription of B117L was detected at 4 hpi and remained stable until 24 hpi (Fig. 6). The pattern of expression of the well-characterized ASFV early protein p30 (CP204L) and the late protein p72 (B646L) has been previously described and is used here as a reference of early and late transcription profiles, respectively. Expression of B117L was detected throughout with a similar kinetics as that of the late protein p72. Therefore, our results indicate that the ASFV B117L gene encodes for a protein that is expressed late during the virus replication cycle.

ASFV B117 localizes in the ER upon cell expression and adopts an N_{out}/C_{in} membrane topology dictated by the single transmembrane domain

The previous structural, phylogenetic and evolutionary analyses suggest a functional role for the MD of B117L, not required at the initial stages of the replication cycle. In principle, this structural IMP could insert into the ER-derived inner lipid envelope that wraps the ASFV core, and/or into the outer envelope acquired from the host cell plasma membrane during exit (41, 42). Cell localization predictions using tools that are based on different machine-learning methods: DeepLoc 2.0 (43) and LA(ProtT5) (44), concur in suggesting the localization of this protein in the ER.

To test these predictions, we next determined experimentally the cell localization of the B117L protein (Georgia isolate) upon expression in HEK293T and HeLa cells (Figs. 7 and S1). Confocal microscopy images of cells transfected with B117L-GFP constructs and markers for the plasma membrane (mCherry-Mem), mitochondria (mCherry-Mito-7), or ER (BiP-mCherry) exhibited a pattern consistent with ER localization (Figs. 7A and S1, left panels). Image analyses to calculate the correlation Pearson indexes confirmed robust co-localization of the expressed B117-GFP construct with soluble (BiP-mCherry) or membrane (mCherry-sec61β) ER markers, which was dependent on the B117L moiety in both cell lines. In contrast, B117L-GFP emission did not correlate with fluorescence emitted by the plasma membrane or mitochondrial markers (Figs. 7A and S1, right panels).

Thus, even in the absence of a conspicuous SP, B117L expressed in cells displayed strong tendency to localize in the ER. Remarkably, some HEK293T and HeLa cells expressing the B117L-GFP construct displayed formation of OSER structures, a phenomenon observed more frequently upon transfection with higher quantities of DNA (Figs. 7B and S2) (30, 45). ER restructuring due to OSER formation was supported by the fact that the soluble ER marker BiP-mCherry appeared to be retained within the lumen of the formed structures, hence, the ER seemed to collapse without membrane rupture as previously described (30). Moreover, OSERs were not observed when the GFP was positioned at the N-terminus (GFP-B117L construct); nor when BiP-mCherry was co-expressed with B117L devoid of tags (Figs. 7B and S2). Reportedly, the GFP tag can induce OSER formation upon overexpression of IMPs, but only when exposed to the cytosolic side of the ER (30, 45). Thus, OSER formation detected upon B117L-GFP

438 expression was dependent on the GFP tag and consistent with an N_{out}/C_{in} topology in
439 accordance to the one predicted by the DeepTMHMM program (Fig. 1A).

440 We next questioned whether the predicted TMH section was the major
441 determinant of the membrane topology adopted by the B117L gene encoded protein.
442 Truncation of N-terminal sequences did not seem to alter the localization or topology of
443 the expressed protein (Fig. S3). Replacing the B117L-GFP TMH with that of
444 sec61γ, which is expected to integrate into the ER membrane with an opposite N_{in}/C_{out}
445 topology (30), interfered with OSER formation (Fig 7B). Thus, it appears that the TMH
446 section is primarily responsible for the N_{out}/C_{in} membrane topology adopted by the
447 B117L gene encoded protein at the ER membrane.

448 Finally, using an anti-GFP tag antibody, we performed a Western-Blot analysis to
449 establish the oligomerization state of the expressed protein (Fig. 7C). To avoid protein
450 complexes formed within OSERs (30, 45), these experiments were carried out using the
451 GFP-B117L fusion devoid of OSER formation capacity. Oligomers were not observed in
452 SDS-solubilized samples of GFP or GFP-B117L incubated at 95 ºC, which exhibited in
453 gel-electrophoresis protein bands that migrated according to their expected MWs, 27 and
454 40 kDa, respectively (Fig. 7C, left panel). In contrast, incubation at 37 ºC preserved a
455 native, fluorescent form of the expressed GFP (46), as well as SDS-resistant oligomeric
456 forms of the GFP-B117L protein (Fig. 7C, right panel). However, due to the fact that the
457 electrophoretic mobility of proteins fused to GFP can be strongly modified by the overall
458 hydrophobicity of their sequence (47), it was difficult to infer the MWs of those
459 complexes.

460 **Permeabilization of ER model membranes by the TMH of B117L**

461 The previous ectopic expression results support efficient incorporation of the
462 ASFV B117L gene product as a single TMH resident ER protein, potentially forming
463 homo-oligomers. Thus, it is conceivable that oligomers of this protein incorporate into
464 the ER-derived inner envelope during ASFV morphogenesis. Given its late expression
465 profile, small size, low abundance (0.16 % of the virion protein mass (11)) and the
466 conservation of aliphatic/aromatic residues within the MD, we hypothesized that this
467 protein might bear a viroporin-like activity, similar to that of the structural proteins
468 Influenza A virus M2 (48) or SARS-CoV E (49).

469 To prove that hypothesis, we first sought to test the possible pore-forming activity
470 of B117L MD. Pore-forming domains of viroporins are known to fold in membranes
471 establishing functionally relevant channel structures, even when assayed in isolation, i.e.,
472 in the absence of other protein regions (50-54). Thus, we designed three partially
473 overlapping peptides, PB117L-1, PB117L-2 and PB117L-3, which encompassed the MD
474 sequence (Fig. 8A). To determine the effects of the peptides on the membrane
475 permeability barrier, we performed permeabilization assays using μm-sized Giant
476 Unilamellar Vesicles (GUVs) that mimicked the ER (53, 54). We further compared the
477 effects at neutral and low pH, emulating conditions before and after entry of the ASFV
478 through the endocytic route (55). To illustrate this single-vesicle approach, Figure 8B
479 displays selected images of vesicles obtained by confocal fluorescence microscopy. All
480 samples exhibited comparable circular morphologies, indicating the preservation of the
481 surrounding bilayer irrespective of the treatment (Fig. 8B). However, in comparison with
482 control untreated GUVs, or GUVs treated with peptides PB117L-1 or PB117L-3, the
483 internal volume of the GUV treated with PB117L-2 at pH 5.0 appeared marked with the

484 externally added fluorescent probe Alexa Fluor 488, indicative of membrane
485 permeabilization.

486 Panels C and D in Figure 8 display single vesicle quantification of these effects
487 and the mean number of permeabilized vesicles, respectively. Untreated vesicles and
488 vesicles that were treated with PB117L-1 did not show significant levels of
489 permeabilization. In contrast, samples treated with PB117L-2 showed low levels of
490 permeabilization at neutral pH that became significant at pH 5.0, whereas the peptide
491 PB117L-3 appeared to induce low levels of permeabilization that were comparable at
492 both pHs. An increase in membrane permeability is not observed in GUVs that contain
493 non-lytic transmembrane domains of class II viroporins (53, 54) or other TMHs (56, 57)
494 and, therefore, the data displayed in Figures 8C and D support the potential pore-forming
495 activity of B117L TMH.

496 **Sequence specificity of the pore-domain structure-function**

497 To gather more evidence supporting the pore-forming activity of B117L TMH,
498 we next characterized in more detail the structure and activity of the PB117L-2 peptide
499 (Fig. 9). In addition, to rule out possible effects arising from nonspecific hydrophobic
500 interactions with membranes, a side-by-side comparison was performed with PB117L-
501 2scr, a peptide designed with the same amino acid composition, but scrambled sequence
502 (sequences compared in Fig. 9A).

503 First, we compared the structures adopted by these peptides in ER-like
504 membranes by means of IR spectroscopy (Fig. 9B). The amide-I band of PB117L-2
505 inserted into membranes at pH 7.4 or 5.0 exhibited main absorption centered at ca. 1654
506 cm^{-1} (peak I) indicating the adoption by the peptide backbone of a main α-helical

structure (58). This would be consistent with the predicted TMH role of the sequence (Fig. 1), and its involvement in the induction of membrane permeability. The presence of smaller bands centered at 1642 cm-1 (peak II) and 1630 cm-1 (peak III), reflects the contributions of inter-helix interactions (59) and solvated helices (60), respectively. In contrast, the amide-I band of PB117L-2scr at pH7.4 displayed pronounced absorption at ca. 1625 cm^{-1} (peak IV), ascribed to extended-aggregated chains (58). Therefore, the presence of this band evidenced a defect for this peptide in membrane folding. Notably, this band was the main component at pH 5.0, consistent with a higher unfolding degree under these conditions.

Next, to demonstrate the existence of a sequence-specific ion-channel (IC) activity we compared both peptides in electrophysiology measurements carried out on planar membranes mimicking the ER lipid composition (Fig. 9C). Recordings at an applied voltage of 50 mV, revealed no events after addition of any of the peptides at pH 7.4. Similarly, we did not register any significant event at pH 5.0 in the presence of the PB117L-2scr peptide. In sharp contrast, recordings in the presence of the PB117L-2 peptide carried out under the same experimental conditions, showed “opening” and “closing” events (current jumps) with various lifetimes, and amplitudes between 1 and 5 pA (20 – 100 pS in conductance), which would be consistent with the formation of ion channels with radii in the range of r ~ 0.5-1 nm. Overall, IC activity data are consistent with a sequence-determined, ion-conducting viroporin function of B117L, which is activated at low pH.

Discussion

Prior to this study there was a complete lack of information about structure-related characteristics and possible functions of the ASFV protein B117L. The gene B117L was predicted to encode for an IMP (10), later defined as a minor component of the ASFV proteome (11). Our study adds to these established notions the possibility that, upon expression, the B117L protein preferentially locates at the ER, organized therein with its small globular ectodomain exposed to the lumen of the organelle, and amphipathic-hydrophobic sequences inserted into its membrane. These latter sequences would compose the MD, defined in this study as an "amphipathic-strand/hydrophobic helix/amphipathic-helix" motif roughly spanning 50 amino acids at the C-terminal end of B117L.

To advance in the knowledge about the functional relevance of this ectodomain-MD partition, we first conducted a comprehensive evolutionary analysis and found that negative selection is the evolutionary force driving the selection of B117L gene, consistent with the evolutionary profile reported in other ASFV genes (A151R, A859L, A104R, E165R , EP296R, and H108R) (26 ,61, 62, 63, 64, 65), indicating the overall evolutionary constraints favoring the conservation of multiple sites of B117L protein. The evolutionary analysis identified a total of 11 residues under negative selection, 7 within the ectodomain and 4 within the MD. Considering the lack of knowledge about this protein, the relevance of this result suggests that these residues may represent critical sites necessary for the structure and/or function of this protein. The analysis performed also supported the high conservation of the MD, stressing the relevance of this domain in the function of this protein.

As a part of the strategy to predict the evolution of this protein, we used two algorithms specialized in the detection of positive selection in the branches. Our results suggested that one of the representative lineages used in this study, evolved as a result of positive selection of ectodomain residues. In the light of these results, we may propose that, besides the common ones performed by the MD, there could be other or different molecular functions associated with the B117L ectodomain in other distant isolates. In this context, future studies could conduct side by side comparisons among different forms of B117L.

The cell expression experiments conducted in this study support the incorporation of B117L into the ER membrane adopting a defined N_{out}/C_{in} topology, even in the absence of a canonical SP. However, we cannot exclude that B117L may be in the ER when expressed alone because it has misfolded or cannot assemble with other viral proteins. Interestingly, prediction of subcellular localization using DeepLoc 2.0 (43) and LA(ProtT5) (44) tools also supported B117L localization in the ER.

Elucidating the mechanism of single pass B117L biogenesis is beyond the scope of this study. The existence a weakly hydrophobic, non-canonical SP undetected by the available prediction tools, which could initiate translocation as a type I IMP cannot be excluded at this point. Even though, the observation that B117L expressed with deleted ectodomain sequences seem to adopt similar N_{out}/C_{in} topologies strongly argues against that possibility (Fig. S3). Alternatively, we speculate that either the cell machinery used by N_{out}/C_{in} type III IMPs, or mechanisms mediated by unknown factors, could be involved in ER targeting of B117L and insertion of its TMH (66). Thus, one possibility explaining ectodomain diversity at the 31-34 hotspot is that its sequence-structure defines

574 different strategies-partners for selective targeting to the ER membrane and its retention
575 therein.

576 Furthermore, electron tomography data support the assembly of the ASFV inner
577 lipid envelope from ER membrane patches, a process accompanied by the loss of the
578 organelle integrity and release of luminal proteins (41). Thus, ER membrane specificity
579 strongly suggests that the virion inner lipid envelope might be the fate of B117L (42).
580 Conceivably, B117L could also be involved in the ER processing by establishing
581 interactions with other viral factors through the ectodomain. However, the observation
582 that overexpression of the protein does not lead to ER disruption suggests that B117L on
583 its own does not destabilize-sever the ER membrane.

584 Based on its small size, the high degree of the MD conservation, its incorporation
585 at low membrane densities into virions, and the low pH-activated pore-forming/ion-
586 channel activities of the TMH-based helical peptide, we rather support a viroporin-like
587 assistant role for B117L during virus entry through the endocytic route. Members of the
588 'Viroporin' family can be generally classified as integral membrane miniproteins bearing
589 the capacity to permeabilize membranes to different solutes (67, 68). In many instances
590 they constitute nonstructural proteins, which are nonessential for virus growth. However,
591 as virulence factors, they may assist viral egress and propagation following a variety of
592 mechanisms that include direct restructuring of cell membrane systems, or indirect effects
593 to manipulate cell death mechanisms and innate immune responses. Notwithstanding the
594 previous generalization, the presence of structural miniproteins that incorporate into the
595 viral envelope and display a viroporin-like activity in response to different stimuli is not
596 uncommon (49, 50, 69). Most prominently, the low pH-activated, proton-conducting

activity of M2 proteins from Influenza A and B viruses (A/M2 and BM2, respectively) appears to be crucial during entry through the endocytic route, to allow the acidification of the virion core and facilitate disassembly of the ribonucleoprotein complexes (70).

Supporting an analogous functional role during ASFV entry, B117L shares a number of structural similarities with A/M2 (71, 72): (i) both appear to be single-pass, type III integral membrane proteins; (ii) both comprise an N-terminal ectodomain, a middle TMH, and a C-terminal amphipatic helix; and (iii) in both instances the TMH assembles the membrane channel. However, in contrast to the proton-selective A/M2, B117L pore-forming domain showed only weak discrimination for ions and small charged solutes. Moreover, ASFV infection was not inhibited in the presence of amantadine (data not shown), an efficient inhibitor of Influenza A virus infection targeting A/M2, which is however inefficient against Influenza B viruses (70). The different amino acid composition of the A/M2 and BM2 pore-forming domains was invoked to explain the inability of this channel blocker to inhibit cell infection by Influenza B viruses (70). Thus, the presence of yet more divergent sequences could explain the lack of effect of amantadine in the case of the ASFV.

In addition, deletion of B117L gene from the genome of the parental ASFV strain Georgia was attempted using previously designed methods performed in our laboratory for successful deletion of individual ASFV genes (4-6, 9, 15-17, 26, 61-65). However, after several attempts we were able to get only a mixed virus population that could be observed by next-generation sequencing, but never a pure population of a recombinant virus lacking B117L. This suggests that some of the potential critical molecular functions of B117L could be complemented from the presence of B117L in other viral parental

genomes. In other words, the fact that a virus lacking the B117L gene could not be produced in purity supports that B117L function must be retained, resulting essential for virus growth.

Determining the molecular function of B117L as a viroporin opens the possibility of the use of antivirals as a potential approach to limit ASFV infection (73). This constitutes the first report of an ASFV protein having viroporin function. In fact, very few proteins encoded by the ASFV genome have any experimentally tested molecular function, having, most of them, only limited functional prediction information from algorism-based analytic programs. To help in defining protein function all of the predicted structures for ASFV proteins has become publicly available, aiding in the effort to determined potential molecular functions of ASFV proteins. However, the functional predictions still require molecular testing. Understating the functional significance of individual proteins aids in the advancement of antiviral drugs, and rationally designed vaccines.

Acknowledgements

We wish to particularly thank Carmen V. Borca-Carrillo for editing the manuscript. This project was partially funded by the Basque Government Grant #IT1449-22 the National Pork Board Project no. 21-137, and by the Foundation for Food and Agriculture Research.

References

1. Costard S, Wieland B, de Glanville W, Jori F, Rowlands R, Vosloo W, Roger F, Pfeiffer DU, Dixon LK. 2009. African swine fever: how can global spread be prevented? Philos Trans R Soc Lond B Biol Sci 364:2683-96.
2. Tulman ER, Delhon GA, Ku BK, Rock DL. 2009. African swine fever virus. Curr Top Microbiol Immunol 328:43-87.
3. Borca MV, Ramirez-Medina E, Silva E, Vuono E, Rai A, Pruitt S, Espinoza N, Velazquez-Salinas L, Gay CG, Gladue DP. 2021. ASFV-G-I177L as an Effective Oral Nasal Vaccine against the Eurasia Strain of Africa Swine Fever. Viruses 27;13(5):765.
4. O'Donnell V, Holinka LG, Gladue DP, Sanford B, Krug PW, Lu X, Arzt J, Reese B, Carrillo C, Risatti GR, Borca MV. 2015. African Swine Fever Virus Georgia Isolate Harboring Deletions of MGF360 and MGF505 Genes Is Attenuated in Swine and Confers Protection against Challenge with Virulent Parental Virus. J Virol 89:6048-56.
5. O'Donnell V, Holinka LG, Sanford B, Krug PW, Carlson J, Pacheco JM, Reese B, Risatti GR, Gladue DP, Borca MV. 2016. African swine fever virus Georgia isolate harboring deletions of 9GL and MGF360/505 genes is highly attenuated in swine but does not confer protection against parental virus challenge. Virus Res 221:8-14.
6. O'Donnell V, Risatti GR, Holinka LG, Krug PW, Carlson J, Velazquez-Salinas L, Azzinaro PA, Gladue DP, Borca MV. 2017. Simultaneous Deletion of the 9GL and UK Genes from the African Swine Fever Virus Georgia 2007 Isolate Offers

Increased Safety and Protection against Homologous Challenge. J Virol. 16;91(1):e01760-16.

7. Monteagudo PL, Lacasta A, Lopez E, Bosch L, Collado J, Pina-Pedrero S, Correa-Fiz F, Accensi F, Navas MJ, Vidal E, Bustos MJ, Rodriguez JM, Gallei A, Nikolin V, Salas ML, Rodriguez F. 2017. BA71DeltaCD2: a New Recombinant Live Attenuated African Swine Fever Virus with Cross-Protective Capabilities. J Virol. 13;91(21):e01058-17
8. Chen W, Zhao D, He X, Liu R, Wang Z, Zhang X, Li F, Shan D, Chen H, Zhang J, Wang L, Wen Z, Wang X, Guan Y, Liu J, Bu Z. 2020. A seven-gene-deleted African swine fever virus is safe and effective as a live attenuated vaccine in pigs. Sci China Life Sci 63:623-634.
9. Gladue DP, Ramirez-Medina E, Vuono E, Silva E, Rai A, Pruitt S, Espinoza N, Velazquez-Salinas L, Borca MV. 2021. Deletion of the A137R Gene from the Pandemic Strain of African Swine Fever Virus Attenuates the Strain and Offers Protection against the Virulent Pandemic Virus. J Virol 95:e0113921.
10. Yanez RJ, Rodriguez JM, Nogal ML, Yuste L, Enriquez C, Rodriguez JF, Vinuela E. 1995. Analysis of the complete nucleotide sequence of African swine fever virus. Virology 208:249-78.
11. Alejo A, Matamoros T, Guerra M, Andres G. 2018. A Proteomic Atlas of the African Swine Fever Virus Particle. J Virol. 12;92(23):e01293-18.
12. Tamura K. 1992. Estimation of the number of nucleotide substitutions when there are strong transition-transversion and G+C-content biases. Mol Biol Evol 9:678-87.

687 13. Edgar RC. 2004. MUSCLE: a multiple sequence alignment method with reduced
688 time and space complexity. BMC Bioinformatics 5:113.
689 14. Kumar S, Stecher G, Li M, Knyaz C, Tamura K. 2018. MEGA X: Molecular
690 Evolutionary Genetics Analysis across Computing Platforms. Mol Biol Evol
691 35:1547-1549.
692 15. Vuono EA, Ramirez-Medina E, Pruitt S, Rai A, Espinoza N, Silva E, Velazquez-
693 Salinas L, Gladue DP, Borca MV. 2022. Deletion of the ASFV dUTPase Gene
694 E165R from the Genome of Highly Virulent African Swine Fever Virus Georgia
695 2010 Does Not Affect Virus Replication or Virulence in Domestic Pigs. Viruses
696 14:1409.
697 16. Ramirez-Medina E, Vuono EA, Pruitt S, Rai A, Espinoza N, Valladares A, Silva
698 E, Velazquez-Salinas L, Borca MV, Gladue DP. 2022. Deletion of African Swine
699 Fever Virus Histone-like Protein, A104R from the Georgia Isolate Drastically
700 Reduces Virus Virulence in Domestic Pigs. Viruses. 22;14(5):1112.
701 17. Ramirez-Medina E, Vuono E, Rai A, Pruitt S, Espinoza N, Velazquez-Salinas L,
702 Pina-Pedrero S, Zhu J, Rodriguez F, Borca MV, Gladue DP. 2022. Deletion of
703 E184L, a Putative DIVA Target from the Pandemic Strain of African Swine Fever
704 Virus, Produces a Reduction in Virulence and Protection against Virulent
705 Challenge. J Virol 96:e0141921.
706 18. Velazquez-Salinas L, Zarate S, Eberl S, Gladue DP, Novella I, Borca MV. 2020.
707 Positive Selection of ORF1ab, ORF3a, and ORF8 Genes Drives the Early
708 Evolutionary Trends of SARS-CoV-2 During the 2020 COVID-19 Pandemic.
709 Front Microbiol 11:550674.

19. Weaver S, Shank SD, Spielman SJ, Li M, Muse SV, Kosakovsky Pond SL. 2018. Datamonkey 2.0: A Modern Web Application for Characterizing Selective and Other Evolutionary Processes. Mol Biol Evol 35:773-777.
20. Kosakovsky Pond SL, Frost SD. 2005. Not so different after all: a comparison of methods for detecting amino acid sites under selection. Mol Biol Evol 22:1208-22.
21. Murrell B, Wertheim JO, Moola S, Weighill T, Scheffler K, Kosakovsky Pond SL. 2012. Detecting individual sites subject to episodic diversifying selection. PLoS Genet 8:e1002764.
22. Spielman SJ, Weaver S, Shank SD, Magalis BR, Li M, Kosakovsky Pond SL. 2019. Evolution of Viral Genomes: Interplay Between Selection, Recombination, and Other Forces. Methods Mol Biol 1910:427-468.
23. Smith MD, Wertheim JO, Weaver S, Murrell B, Scheffler K, Kosakovsky Pond SL. 2015. Less is more: an adaptive branch-site random effects model for efficient detection of episodic diversifying selection. Mol Biol Evol 32:1342-53.
24. Murrell B, Weaver S, Smith MD, Wertheim JO, Murrell S, Aylward A, Eren K, Pollner T, Martin DP, Smith DM, Scheffler K, Kosakovsky Pond SL. 2015. Gene-wide identification of episodic selection. Mol Biol Evol 32:1365-71.
25. Kosakovsky Pond SL, Posada D, Gravenor MB, Woelk CH, Frost SD. 2006. Automated phylogenetic detection of recombination using a genetic algorithm. Mol Biol Evol 23:1891-901.

731 26. Ramirez-Medina E, Vuono EA, Pruitt S, Rai A, Espinoza N, Velazquez-Salinas L,
732 Gladue DP, Borca MV. 2021. Evaluation of an ASFV RNA Helicase Gene
733 A859L for Virus Replication and Swine Virulence. Viruses 14(1):10.
734 27. Gladue DP, Holinka LG, Largo E, Fernandez Sainz I, Carrillo C, O'Donnell V,
735 Baker-Branstetter R, Lu Z, Ambroggio X, Risatti GR, Nieva JL, Borca MV. 2012.
736 Classical swine fever virus p7 protein is a viroporin involved in virulence in
737 swine. J Virol 86:6778-91.
738 28. Largo E, Gladue DP, Huarte N, Borca MV, Nieva JL. 2014. Pore-forming activity
739 of pestivirus p7 in a minimal model system supports genus-specific viroporin
740 function. Antiviral Res 101:30-6.
741 29. Zurek N, Sparks L, Voeltz G. 2011. Reticulon short hairpin transmembrane
742 domains are used to shape ER tubules. Traffic 12:28-41.
743 30. Snapp EL, Hegde RS, Francolini M, Lombardo F, Colombo S, Pedrazzini E,
744 Borgese N, Lippincott-Schwartz J. 2003. Formation of stacked ER cisternae by
745 low affinity protein interactions. J Cell Biol 163:257-69.
746 31. Apellaniz B, Nieva JL, Schwille P, Garcia-Saez AJ. 2010. All-or-none versus
747 graded: single-vesicle analysis reveals lipid composition effects on membrane
748 permeabilization. Biophys J 99:3619-28.
749 32. Apellaniz B, Garcia-Saez AJ, Huarte N, Kunert R, Vorauer-Uhl K, Katinger H,
750 Schwille P, Nieva JL. 2010. Confocal microscopy of giant vesicles supports the
751 absence of HIV-1 neutralizing 2F5 antibody reactivity to plasma membrane
752 phospholipids. FEBS Lett 584:1591-6.

753 33. Arrondo JL, Goni FM. 1999. Structure and dynamics of membrane proteins as
754 studied by infrared spectroscopy. Prog Biophys Mol Biol 72:367-405.
755 34. Largo E, Queralt-Martin M, Carravilla P, Nieva JL, Alcaraz A. 2021. Single-
756 molecule conformational dynamics of viroporin ion channels regulated by lipid-
757 protein interactions. Bioelectrochemistry 137:107641.
758 35. Mistry J, Chuguransky S, Williams L, Qureshi M, Salazar GA, Sonnhammer
759 ELL, Tosatto SCE, Paladin L, Raj S, Richardson LJ, Finn RD, Bateman A. 2021.
760 Pfam: The protein families database in 2021. Nucleic Acids Res 49:D412-D419.
761 36. Holgersen EM, Gandhi S, Zhou Y, Kim J, Vaz B, Bogojeski J, Bugno M, Shalev
762 Z, Cheung-Ong K, Goncalves J, O'Hara M, Kron K, Verby M, Sun M, Kakaradov
763 B, Delong A, Merico D, Deshwar AG. 2021. Transcriptome-Wide Off-Target
764 Effects of Steric-Blocking Oligonucleotides. Nucleic Acid Ther 31:392-403.
765 37. Senior AW, Evans R, Jumper J, Kirkpatrick J, Sifre L, Green T, Qin C, Zidek A,
766 Nelson AWR, Bridgland A, Penedones H, Petersen S, Simonyan K, Crossan S,
767 Kohli P, Jones DT, Silver D, Kavukcuoglu K, Hassabis D. 2020. Improved
768 protein structure prediction using potentials from deep learning. Nature 577:706-
769 710.
770 38. Kyte J, Doolittle RF. 1982. A simple method for displaying the hydropathic
771 character of a protein. J Mol Biol 157:105-32.
772 39. Monne M, Nilsson I, Elofsson A, von Heijne G. 1999. Turns in transmembrane
773 helices: determination of the minimal length of a "helical hairpin" and derivation
774 of a fine-grained turn propensity scale. J Mol Biol 293:807-14.

775 40. Aslanyan L, Avagyan H, Karalyan Z. 2020. Whole-genome-based phylogeny of
776 African swine fever virus. Vet World 13:2118-2125.
777 41. Suarez C, Andres G, Kolovou A, Hoppe S, Salas ML, Walther P, Krijnse Locker
778 J. 2015. African swine fever virus assembles a single membrane derived from
779 rupture of the endoplasmic reticulum. Cell Microbiol 17:1683-98.
780 42. Salas ML, Andres G. 2013. African swine fever virus morphogenesis. Virus Res
781 173:29-41.
782 43. Thumuluri V, Almagro Armenteros JJ, Johansen AR, Nielsen H, Winther O.
783 2022. DeepLoc 2.0: multi-label subcellular localization prediction using protein
784 language models. Nucleic Acids Res 50:W228-34.
785 44. Stark H, Dallago C, Heinzinger M, Rost B. 2021. Light attention predicts protein
786 location from the language of life. Bioinform Adv 1:vbab035.
787 45. Costantini LM, Fossati M, Francolini M, Snapp EL. 2012. Assessing the tendency
788 of fluorescent proteins to oligomerize under physiologic conditions. Traffic
789 13:643-9.
790 46. Inouye S, Tsuji FI. 1994. Aequorea green fluorescent protein. Expression of the
791 gene and fluorescence characteristics of the recombinant protein. FEBS Lett
792 341:277-80.
793 47. Aoki T, Takahashi Y, Koch KS, Leffert HL, Watabe H. 1996. Construction of a
794 fusion protein between protein A and green fluorescent protein and its application
795 to Western blotting. FEBS Letters 384:193-197.
796 48. Pinto LH, Holsinger LJ, Lamb RA. 1992. Influenza virus M2 protein has ion
797 channel activity. Cell 69:517-28.

798 49. Nieto-Torres JL, DeDiego ML, Verdia-Baguena C, Jimenez-Guardeno JM, Regla-
799 Nava JA, Fernandez-Delgado R, Castano-Rodriguez C, Alcaraz A, Torres J,
800 Aguilella VM, Enjuanes L. 2014. Severe acute respiratory syndrome coronavirus
801 envelope protein ion channel activity promotes virus fitness and pathogenesis.
802 PLoS Pathog 10:e1004077.
803 50. Acharya R, Carnevale V, Fiorin G, Levine BG, Polishchuk AL, Balannik V,
804 Samish I, Lamb RA, Pinto LH, DeGrado WF, Klein ML. 2010. Structure and
805 mechanism of proton transport through the transmembrane tetrameric M2 protein
806 bundle of the influenza A virus. Proc Natl Acad Sci U S A 107:15075-80.
807 51. Mandala VS, McKay MJ, Shcherbakov AA, Dregni AJ, Kolocouris A, Hong M.
808 2020. Structure and drug binding of the SARS-CoV-2 envelope protein
809 transmembrane domain in lipid bilayers. Nat Struct Mol Biol 27:1202-1208.
810 52. Madan V, Sanchez-Martinez S, Vedovato N, Rispoli G, Carrasco L, Nieva JL.
811 2007. Plasma membrane-porating domain in poliovirus 2B protein. A short
812 peptide mimics viroporin activity. J Mol Biol 374:951-64.
813 53. Largo E, Gladue DP, Torralba J, Aguilella VM, Alcaraz A, Borca MV, Nieva JL.
814 2018. Mutation-induced changes of transmembrane pore size revealed by
815 combined ion-channel conductance and single vesicle permeabilization analyses.
816 Biochim Biophys Acta Biomembr 1860:1015-1021.
817 54. Gladue DP, Largo E, de la Arada I, Aguilella VM, Alcaraz A, Arrondo JLR,
818 Holinka LG, Brocchi E, Ramirez-Medina E, Vuono EA, Berggren KA, Carrillo C,
819 Nieva JL, Borca MV. 2018. Molecular Characterization of the Viroporin Function

820 of Foot-and-Mouth Disease Virus Nonstructural Protein 2B. J Virol
821 12;92(23):e01360-18.
822 55. Hernaez B, Guerra M, Salas ML, Andres G. 2016. African Swine Fever Virus
823 Undergoes Outer Envelope Disruption, Capsid Disassembly and Inner Envelope
824 Fusion before Core Release from Multivesicular Endosomes. PLoS Pathog
825 12:e1005595.
826 56. Torralba J, de la Arada I, Carravilla P, Insausti S, Rujas E, Largo E, Eggeling C,
827 Arrondo JLR, Apellaniz B, Nieva JL. 2020. Cholesterol Constrains the Antigenic
828 Configuration of the Membrane-Proximal Neutralizing HIV-1 Epitope. ACS
829 Infect Dis 6:2155-2168.
830 57. Torralba J, de la Arada I, Partida-Hanon A, Rujas E, Arribas M, Insausti S,
831 Valotteau C, Valle J, Andreu D, Caaveiro JMM, Jimenez MA, Apellaniz B,
832 Redondo-Morata L, Nieva JL. 2022. Molecular recognition of a membrane-
833 anchored HIV-1 pan-neutralizing epitope. Commun Biol 5:1265.
834 58. Arrondo JL, Goni FM. 1999. Structure and dynamics of membrane proteins as
835 studied by infrared spectroscopy. Prog Biophys Mol Biol 72:367-405.
836 59. Vu DM, Myers JK, Oas TG, Dyer RB. 2004. Probing the folding and unfolding
837 dynamics of secondary and tertiary structures in a three-helix bundle protein.
838 Biochemistry 43:3582-9.
839 60. Walsh ST, Cheng RP, Wright WW, Alonso DO, Daggett V, Vanderkooi JM,
840 DeGrado WF. 2003. The hydration of amides in helices; a comprehensive picture
841 from molecular dynamics, IR, and NMR. Protein Sci 12:520-31.

842 61. Ramirez-Medina E, Vuono E, Pruitt S, Rai A, Espinoza N, Valladares A, Spinard
843 E, Silva E, Velazquez-Salinas L, Gladue DP, Borca MV. 2022. ASFV Gene
844 A151R Is Involved in the Process of Virulence in Domestic Swine. Viruses
845 14:1834.
846 62. Ramirez-Medina E, Vuono EA, Pruitt S, Rai A, Espinoza N, Valladares A, Silva
847 E, Velazquez-Salinas L, Borca MV, Gladue DP. 2022. Deletion of African Swine
848 Fever Virus Histone-like Protein, A104R from the Georgia Isolate Drastically
849 Reduces Virus Virulence in Domestic Pigs. Viruses 22;14(5):1112.
850 63. Vuono EA, Ramirez-Medina E, Pruitt S, Rai A, Espinoza N, Silva E, Velazquez-
851 Salinas L, Gladue DP, Borca MV. 2022. Deletion of the ASFV dUTPase Gene
852 E165R from the Genome of Highly Virulent African Swine Fever Virus Georgia
853 2010 Does Not Affect Virus Replication or Virulence in Domestic Pigs. Viruses
854 14:1409.
855 64. Vuono EA, Ramirez-Medina E, Pruitt S, Rai A, Espinoza N, Spinard E,
856 Valladares A, Silva E, Velazquez-Salinas L, Borca MV, Gladue DP. 2022.
857 Deletion of the EP296R Gene from the Genome of Highly Virulent African Swine
858 Fever Virus Georgia 2010 Does Not Affect Virus Replication or Virulence in
859 Domestic Pigs. Viruses 14:1682.H
860 65. Vuono E, Ramirez-Medina E, Silva E, Rai A, Pruitt S, Espinoza N, Valladares A,
861 Velazquez-Salinas L, Gladue DP, Borca MV. 2022. Deletion of the H108R Gene
862 Reduces Virulence of the Pandemic Eurasia Strain of African Swine Fever Virus
863 with Surviving Animals Being Protected against Virulent Challenge. J Virol
864 96:e0054522.

865 66. Hegde RS, Keenan RJ. 2022. The mechanisms of integral membrane protein
866 biogenesis. Nat Rev Mol Cell Biol 23:107-124.
867 67. Nieva JL, Madan V, Carrasco L. 2012. Viroporins: structure and biological
868 functions. Nat Rev Microbiol 10:563-74.
869 68. DiMaio D. 2014. Viral miniproteins. Annu Rev Microbiol 68:21-43.
870 69. Li Y, To J, Verdia-Baguena C, Dossena S, Surya W, Huang M, Paulmichl M, Liu
871 DX, Aguilella VM, Torres J. 2014. Inhibition of the human respiratory syncytial
872 virus small hydrophobic protein and structural variations in a bicelle environment.
873 J Virol 88:11899-914.
874 70. Pinto LH, Lamb RA. 2006. The M2 proton channels of influenza A and B viruses.
875 J Biol Chem 281:8997-9000.
876 71. Lamb RA. 2020. The Structure, Function, and Pathobiology of the Influenza A
877 and B Virus Ion Channels. Cold Spring Harb Perspect Med 2;10(11):a038505.
878 72. Pielak RM, Chou JJ. 2011. Influenza M2 proton channels. Biochim Biophys Acta
879 1808:522-9.
880 73. Scott C, Griffin S. 2015. Viroporins: structure, function and potential as antiviral
881 targets. J Gen Virol 96:2000-2027.
882 74. Pettersen EF, Goddard TD, Huang CC, Couch GS, Greenblatt DM, Meng EC,
883 Ferrin TE. 2004. UCSF Chimera--a visualization system for exploratory research
884 and analysis. J Comput Chem 25:1605-12.

885

886

887 **Figure legends:**

888 **Figure 1: Membrane domain prediction for B117L gene. (A)** Sequence of the B117L
889 gene (Georgia isolate). Residues colored according to the DeepTMHMM prediction
890 displayed below (left panels); blue, red and magenta correspond to the N-terminal outside
891 sequence, the predicted transmembrane helix (TMH, underlined) and the C-terminal
892 inside sequence, respectively. The 3D-structure predicted by AlphaFold is depicted on the
893 right side using the same color code and inserted into a POPC lipid bilayer with the
894 predicted orientation. **(B)** The B117L sequence on top highlights in green the positions of
895 hydrophobic residues within the segment spanning an amphipatic strand, the hydrophobic
896 helix and an amphipatic helix (underlined and designated as MD). Range and sequences
897 for these membrane-associating elements were predicted from hydropathy plots shown
898 below, which are based on the Kyte-Doolittle scale (38). The 3D model on the right
899 displays side-chains for these residues (depicted in green) and proposes a kink at position
900 Arg95-His96 to allow the insertion of the C-terminal amphipathic helix into the
901 membrane interface facing the cytosol. Lys-67 at the beginning of the TMH is depicted in
902 blue. 3D-structures rendered with Chimera (74).

903 **Figure 2. Diversity of B177L gene among ASFV isolates in nature. (A)** Amino acid
904 alignment showing the diversity of B117L protein among a group of 8 representative
905 ASFV isolates. Conservation plot scores reflect the nature of the change in specific sites.
906 Increased scores reflect substitutions between residues with similar biological properties.
907 MD boundaries are limited by the grey squares. Analysis was conducted in the software
908 Jalview version 2.11.1.7. **(B)** Phylogenetic analysis conducted by maximum likelihood
909 method using the full-length sequence of B117L gene indicates the existence of four

potential phylogenetic groups. Red numbers in the parenthesis indicate the genotype of different strains based on p72 classification.

Figure 3. Evolutionary signatures of B117L gene. (A) Graphic representation of the ratio dN-dS at specific codon sites in the B117L gene of ASFV. MD is highlighted in grey. Asterisks in green and red denote codons evolving under positive or negative selection respectively. Analyses were conducted using the evolutionary algorithms MEME and FEL considering a cutoff value of p=0.1. **(B)** Codon-amino acid alignment showing sites detected under positive selection and at negative selection on the MD. Different nodes represent the codon-amino acid sequence at predicted ancestral sequences. Analysis was conducted by the algorithm SLAC. **(C)** 3D-structure model displaying the positions of detected residues. **(D)** Pairwise distance analysis comparing the nucleotide conservation between the genome and the MD. **(E)** Comparison between synonymous (dS) and nonsynonymous (dN) substitutions rates during the evolution of B117L gene. Significant differences in **(D)** and **(E)** were determined by the unpaired t-test.

Figure 4. Evolutionary branch analysis. (A) aBSREL analysis. Phylogenetic tree showing the dN/dS rates at different branches associated with representative isolates included in this study. Asterisk in isolate Ken05/Tk1, represents the only branch in the tree associated with positive selection. LRT and p-values obtained during the analysis are shown below the branch. Also, the two dN/dS ratio classes inferred in this analysis are shown. In this context, dN/dS ratios <1 or >1 represent values under negative or positive selection respectively. Percentages in the parenthesis represent the proportion of codons sites associated with each class. **(B)** BUSTED analysis. The graphic shows an analysis of

933 the specific codon sites on the branch associated with the isolate Ken05/Tk1, where
934 evidence of the rejection about the constrained and optimized null models (both
935 considering absence of positive selection) was obtained. MD is highlighted in grey. **(C)**
936 The figure shows relevant codon sites predicted by BUSTED analysis, implicated in the
937 potential phenotypic differences predicted on B117L gene of Ken05/Tk1. The 3D-
938 structure predicted by Alphafold for this isolate is shown on the right-side, revealing a
939 similar MD organization and the preservation of a helical structure within the
940 ectodomain. A closer view to this element is displayed below showing the position of the
941 31-34 residues.

942 **Figure 5. Recombination analysis.** Phylogenetic analyses using different segments
943 associated with inferred breakpoints, showing topology incongruences among isolates.
944 Analysis was conducted by the maximum likelihood method. Numbers above internal
945 branches represent bootstrap values (1000 repetitions). Correlations (R2 values) represent
946 comparisons between pairwise distance analysis conducted between isolates using full
947 length B117L sequences and different fragments. Values ranges between 1 and 0
948 represents different degrees of topology incongruence.

949 **Figure 6: Expression profile of B117L gene of ASFV during in vitro infection of**
950 **porcine macrophages.** Reverse transcription followed by qPCR was used to evaluate the
951 expression profile of the B117L gene during in vitro infection at different time points, up
952 to 24 h. As a reference for this analysis, we used qPCRs to specifically detect the
953 expression of genes encoding ASFV proteins p30 (early expression) and p72 (late
954 expression). Additionally, the b-actin gene was used as a control to evaluate the quality
955 and levels of RNA during the infection at different time points.

Figure 7: ER localization of B117L upon cell expression. (A) Expression of the B117L-GFP construct in HEK293T cells and co-localization with markers for the Plasma Membrane, Mitochondria, ER soluble compartment and ER membrane. The plot on the right depicts co-localization levels (Pearson coefficients) as calculated with the ImageJ plugin Coloc 2 program (http://imagej.net/Coloc_2). Measurements were carried out in at least 6 cells as those displayed in the left panels. Bars represent mean values ± SD. **(B)** Structures compatible with OSER formation were observed in cells expressing the GFP tag placed at the C-terminus of B117L (B117-GFP construct), but not when the GFP was placed at the N-terminus (GFP-B117L construct) or when Sec61γ TMH substituted for that of B117L (B117L-Sec61TMH-GFP construct). The panel on the right displays Pearson coefficients consistent with co-localization of all B117L GFP fusions with the ER marker BiP-mCherry. OSER were also absent from cells co-expressing untagged B117L. **(C)** Formation of oligomers in cells transfected with GFP and GFP-B117L constructs (lanes 1 and 2, respectively). Cell extracts were applied to SDS-PAGE and GFP detected by immunoblotting using an anti-GFP antibody. Samples were incubated in running buffer at 95 ºC or 37 ºC for 10 min before electrophoresis (left and right panels, respectively).

Figure 8: Identification of the pore-forming domain of B117L using MD-based peptides (A) Sequence and designation of MD spanning peptides. **(B)** Single ER-GUV permeabilization assay. Micrographs depict Rho-PE-labeled ER-GUVs (orange circumferences) immersed in a solution containing Alexa Fluor 488 (green background). In samples incubated with PB117L-2, the green label diffuses into the lumen of the vesicle indicative of membrane permeabilization. Scale bars correspond to 20 μm in all

micrographs. **(C)** Distribution of single ER-GUVs according to their permeabilization percentage to Alexa Fluor 488 after treatment with the different B117L peptides at pH 7.4 or 5.0. Horizontal bars indicate the median values. **(D)** Percentage of vesicles in the previous samples displaying permeabilization levels higher than 70% (threshold level indicated by the dotted line in the previous panel). Peptides were applied at 200 nM concentration.

Figure 9: Dependency of PB117L-2 structure-function on sequence. (A) Comparison of peptides PB117L-2 and PB117L-2scr (wt sequence scrambled using the server: https://www.bioinformatics.org/sms2/shuffle_protein.html). **(B)** Amide I region IR spectra of PB117L-2 and PB117L-2scr reconstituted in ER-like membranes (peptide-to-lipid ratio, 1:50) at pH 7.4 or 5.0 as indicated in the panels. Absorption band components are depicted with thin traces and their maxima indicated by the Roman numerals (see text for their assignment). **(C)** Ion channel activity in ER-like planar bilayers. Current recordings before (No peptide) and after the addition of peptides PB117L-2 and PB117L-2scr at pH 7.4 or 5.0. Current jumps consistent with ion channel activity can be observed with PB117L-2 at pH 5.0. The applied voltage is 50 mV. The recordings were digitally filtered at 500 Hz using a low-pass 8-pole Bessel filter for better visualization.

A

[1]MGYTIQLDKDGDYCWDEDPTHHDPYMQANATSHVATSYATTSHAATPHAAAHHTFHEPFIKLNLTDKN
-[69]IFNGLGFILIVIFIYLLLITL[89]-QQMLTRHIYNTVQHCVKAHLDSKNLQ[115]

TMH

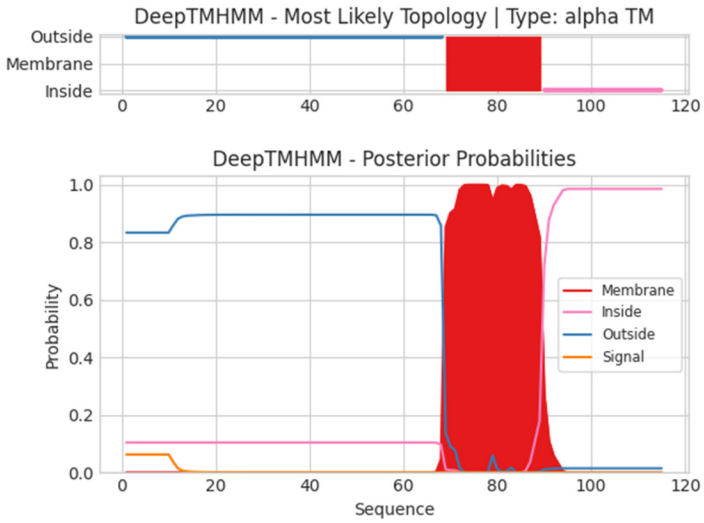

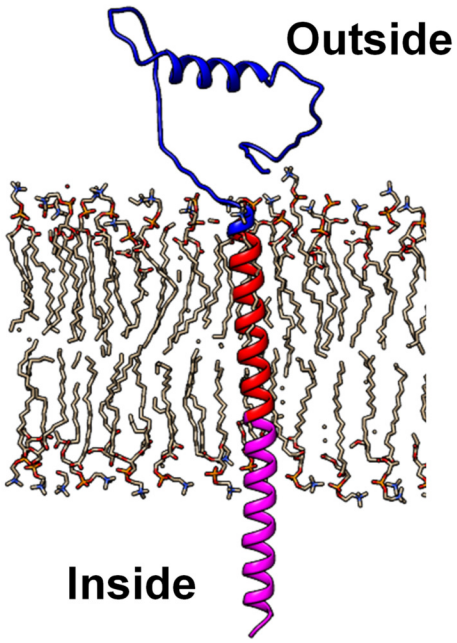

B

[1]MGYTIQLDKDGDYCWDEDPTHHDPYMQANATSHVATSYATTSHAATPHAAAHHTFHEPF-
[60]IKLNLTDKNIFNGLGFILIVIFIYLLLITLQQMLTRHIYNTVQHCVKAHL[109]-DSKNLQ[115]

MD

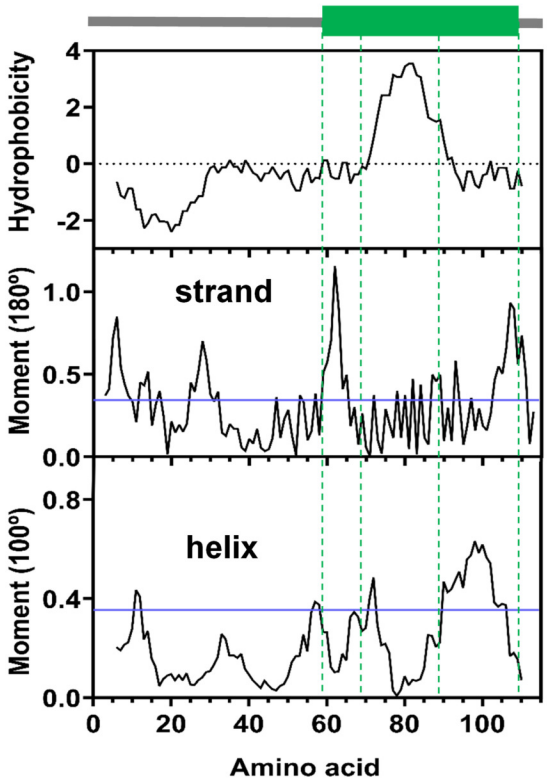

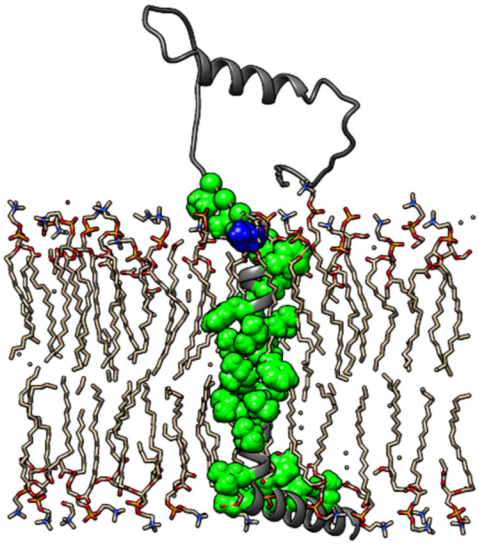

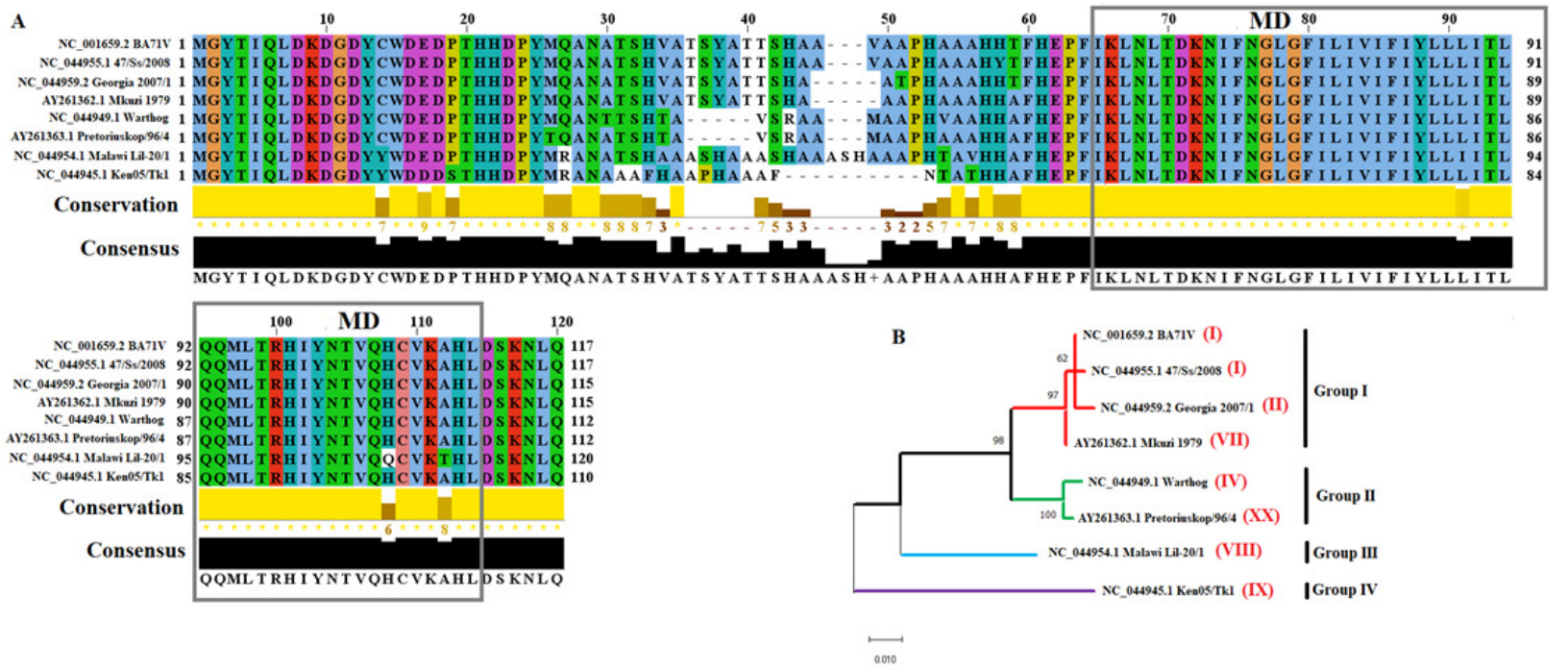
A
MD
NC_001659.2 BA71V
NC_044955.1 47/Ss/2008
NC_044959.2 Georgia 2007/1
AY261362.1 Mkuzi 1979
NC_044949.1 Warthog
AY261363.1 Pretoriuskop/96/4
NC_044954.1 Malawi Lil-20/1
NC_044945.1 Ken05/Tk1
Conservation
Consensus
B
Group I
Group II
Group III
Group IV
0.010

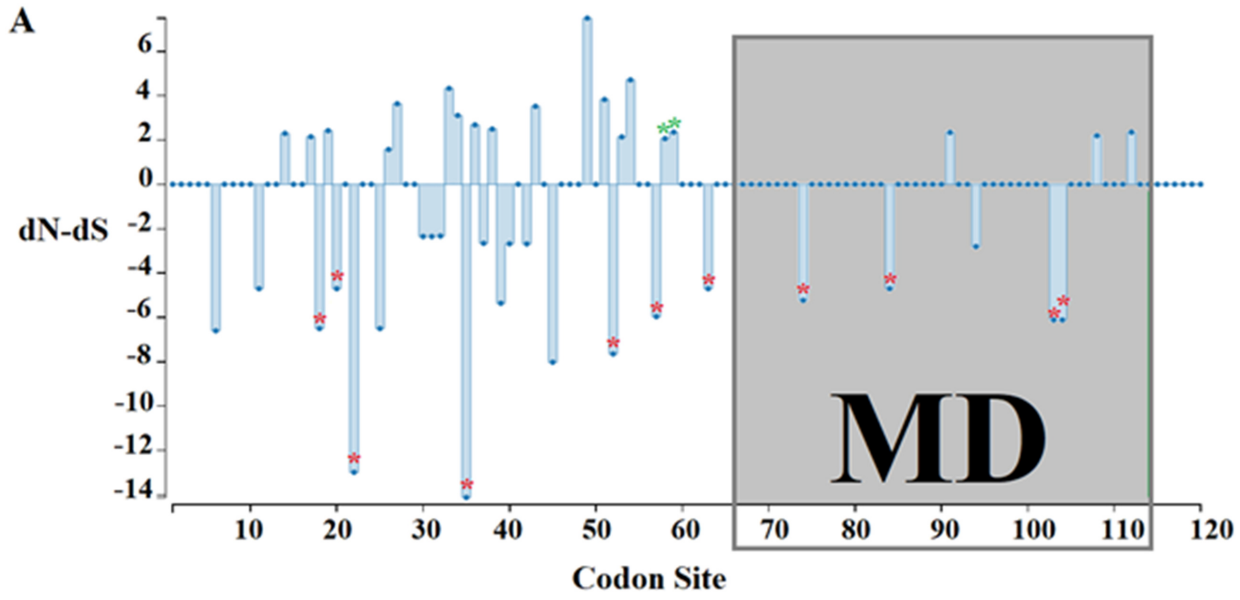
A
dN-dS
Codon Site
MD

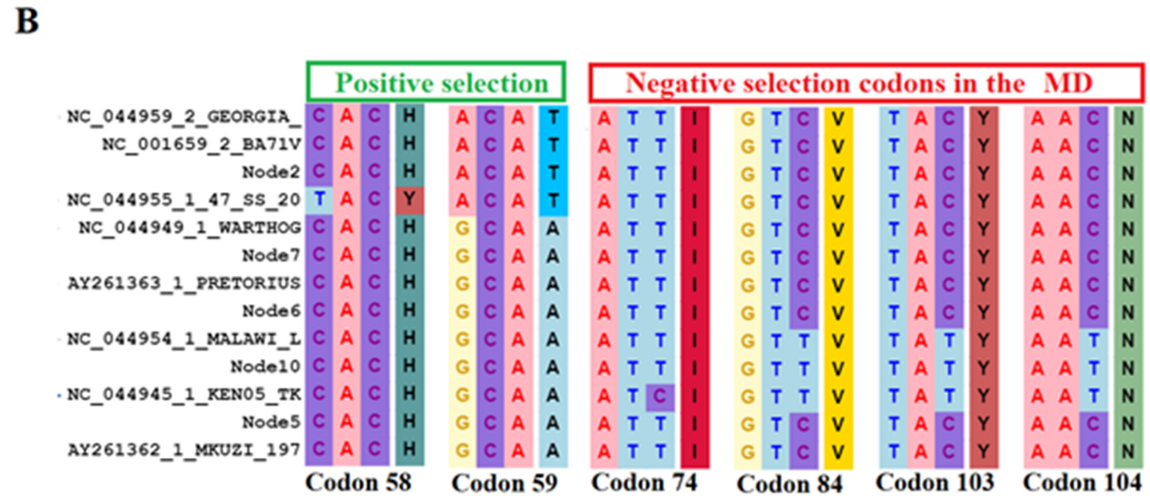
B
Positive selection
Negative selection codons in the MD
NC_044959_2_GEORGIA_
NC_001659_2_BA71V
Node2
NC_044955_1_47_SS_20
NC_044949_1_WARTHOG
Node7
AY261363_1_PRETORIUS
Node6
NC_044954_1_MALAWI_L
Node10
NC_044945_1_KEN05_TK
Node5
AY261362_1_MKUZI_197
Codon 58
Codon 59
Codon 74
Codon 84
Codon 103
Codon 104

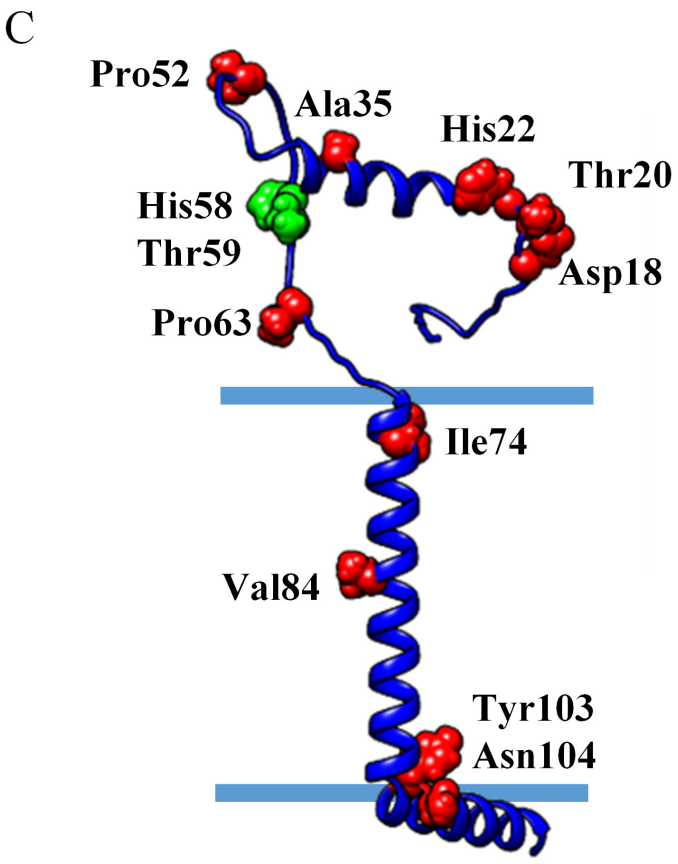
C
Pro52
Ala35
His22
Thr20
His58
Thr59
Asp18
Pro63
Ile74
Val84
Tyr103
Asn104

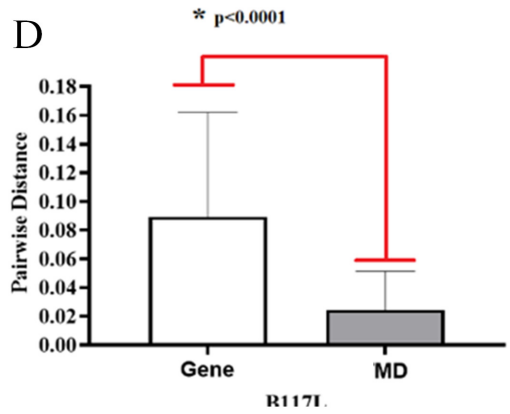
D
* p<0.0001
Pairwise Distance
Gene
MD

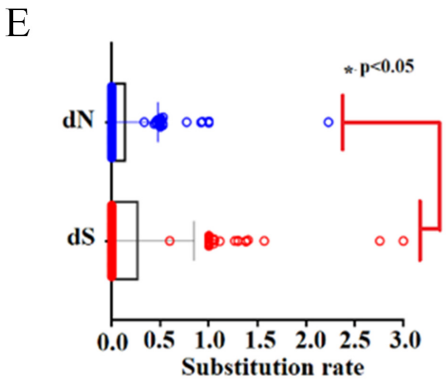
E
* p<0.05
dN
dS
Substitution rate

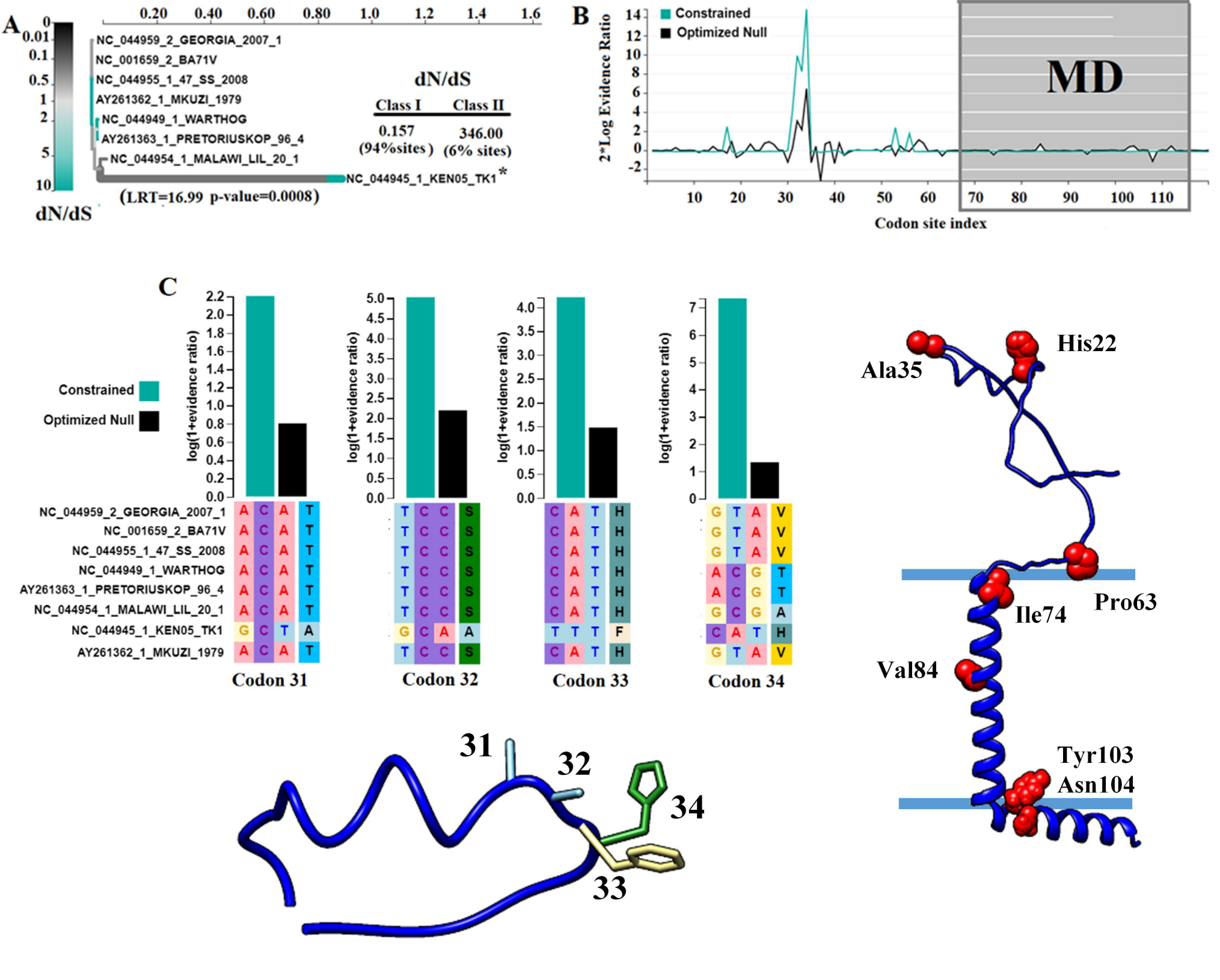
A
dN/dS
NC_044959_2_GEORGIA_2007_1
NC_001659_2_BA71V
NC_044955_1_47_SS_2008
AY261362_1_MKUZI_1979
NC_044949_1_WARTHOG
AY261363_1_PRETORIUSKOP_96_4
NC_044954_1_MALAWI_LIL_20_1
NC_044945_1_KEN05_TK1 *
(LRT=16.99 p-value=0.0008)
dN/dS
Class I
Class II
0.157
(94%sites)
346.00
(6% sites)
B
Constrained
Optimized Null
2*Log Evidence Ratio
MD
Codon site index
C
Constrained
Optimized Null
log(1+evidence ratio)
Codon 31
Codon 32
Codon 33
Codon 34
His22
Ala35
Pro63
Ile74
Val84
Tyr103
Asn104
31
32
33
34

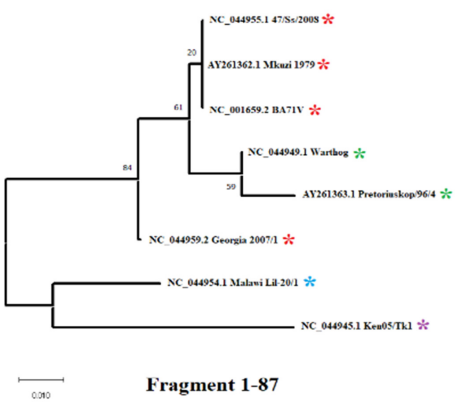

Fragment 1-87
R2=0.7997

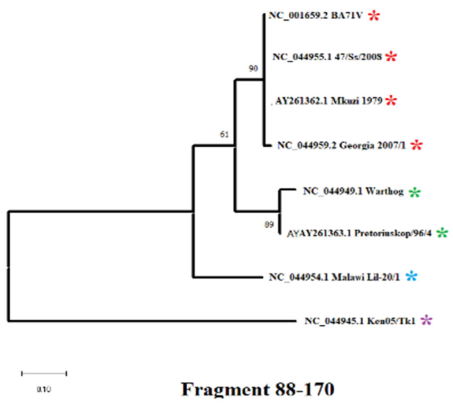

Fragment 88-170
R2=0.9087

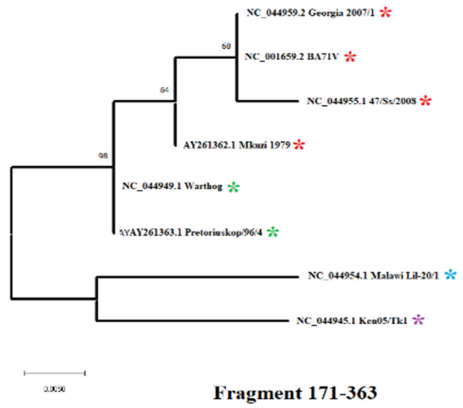

Fragment 171-363
R2=0.8031

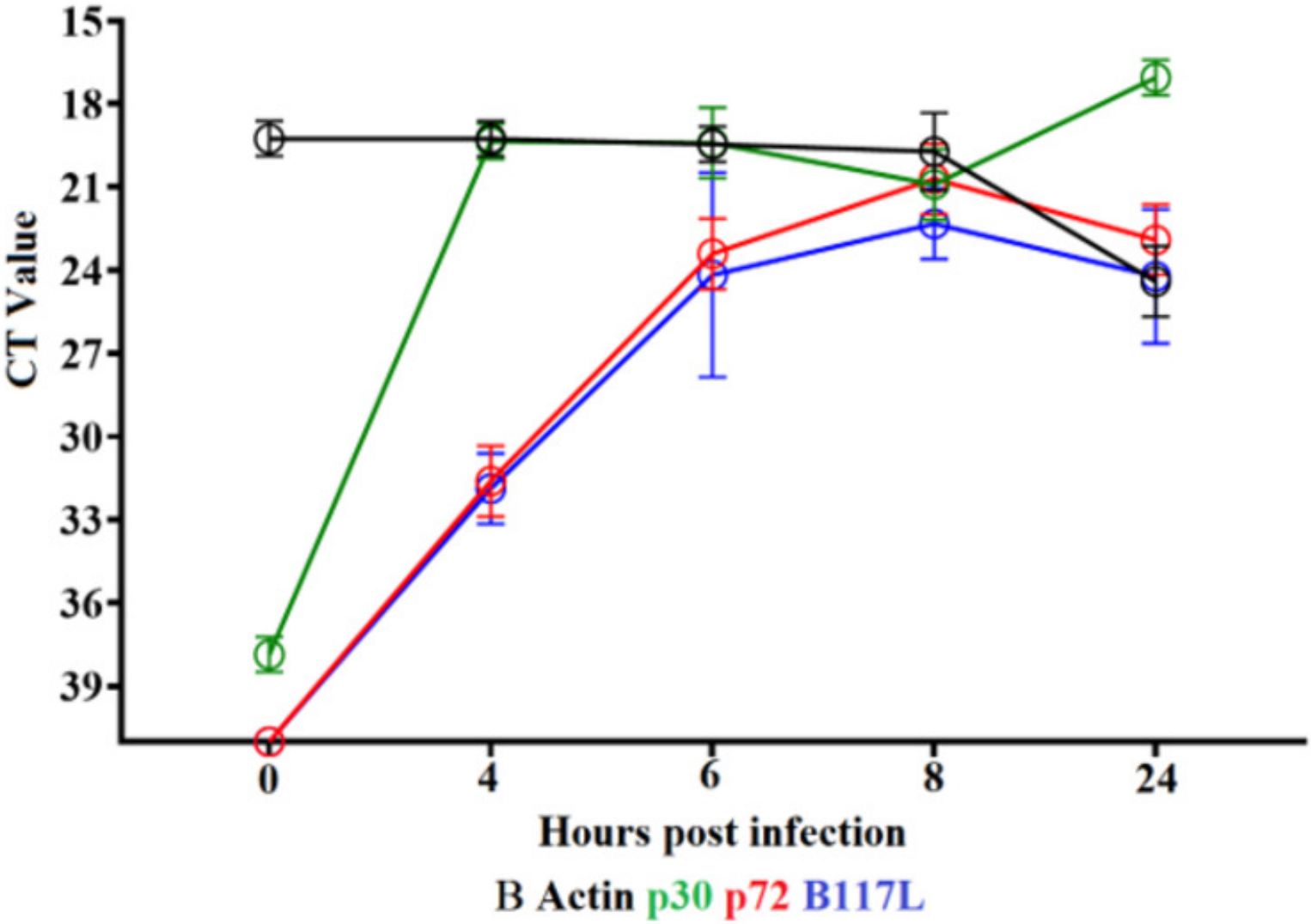
15
18
21
24
27
30
33
36
39
CT Value
0
4
6
8
24
Hours post infection
B Actin p30 p72 B117L

A

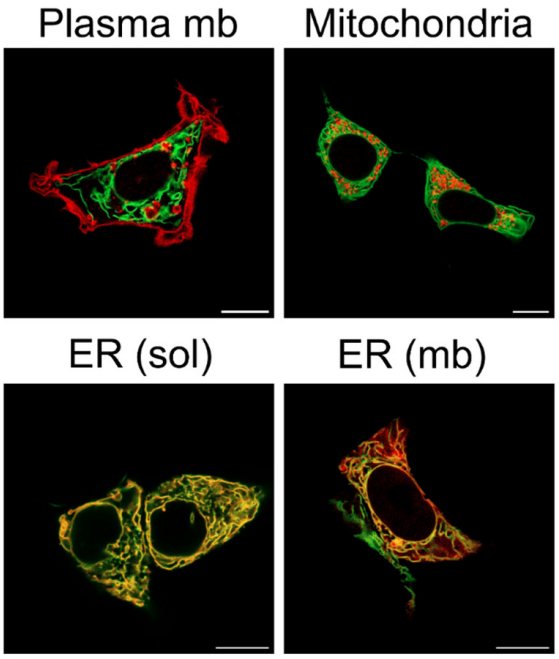
Plasma mb
Mitochondria
ER (sol)
ER (mb)

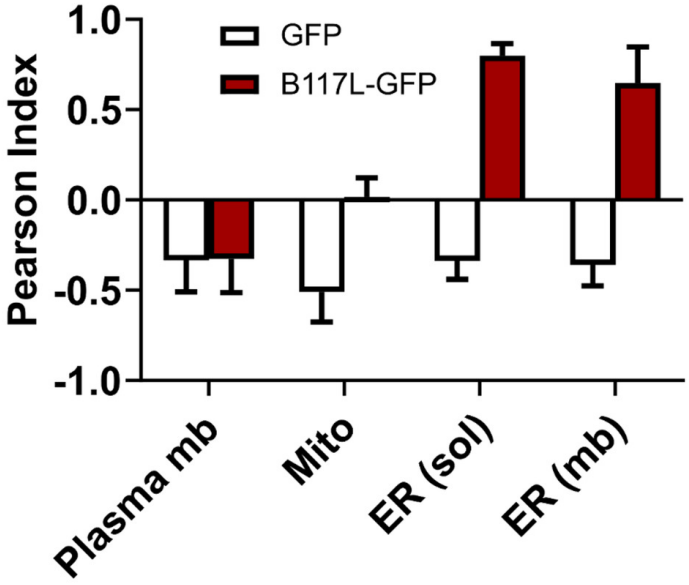
GFP
B117L-GFP
Pearson Index
1.0
0.5
0.0
-0.5
-1.0
Plasma mb
Mito
ER (sol)
ER (mb)

B

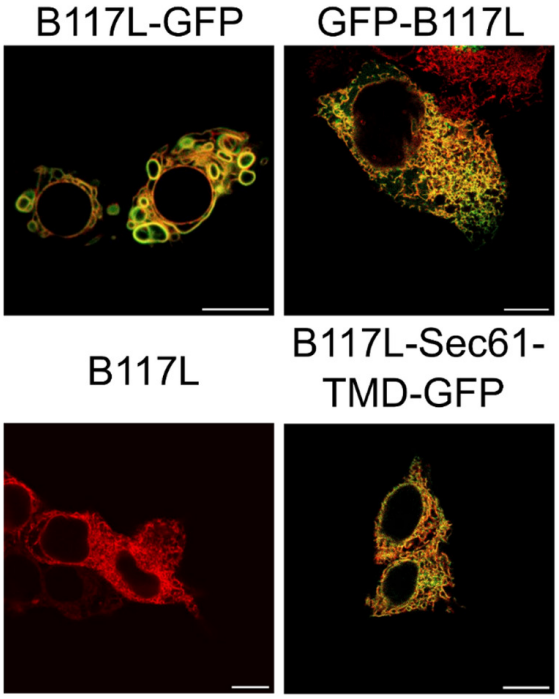
B117L-GFP
GFP-B117L
B117L
B117L-Sec61-TMD-GFP

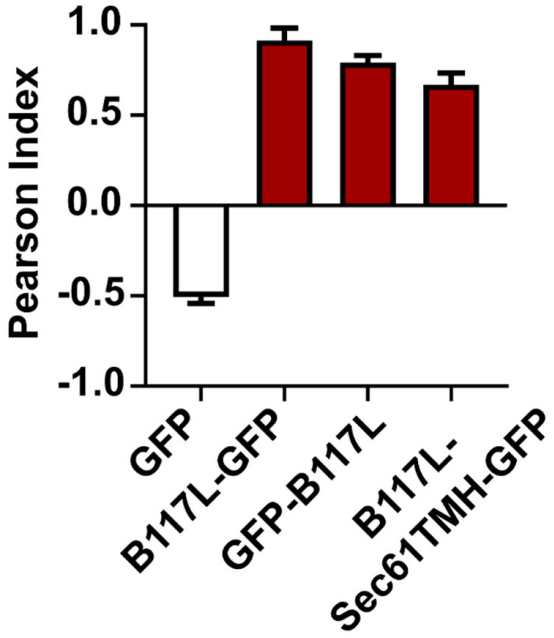
Pearson Index
1.0
0.5
0.0
-0.5
-1.0
GFP
B117L-GFP
GFP-B117L
B117L-Sec61TMH-GFP

C

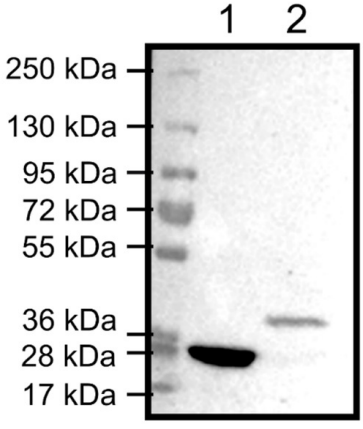
1
2
250 kDa
130 kDa
95 kDa
72 kDa
55 kDa
36 kDa
28 kDa
17 kDa

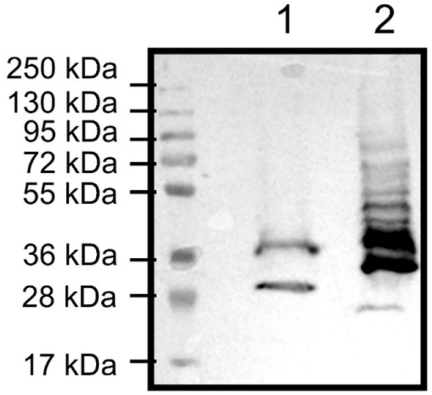
1
2
250 kDa
130 kDa
95 kDa
72 kDa
55 kDa
36 kDa
28 kDa
17 kDa

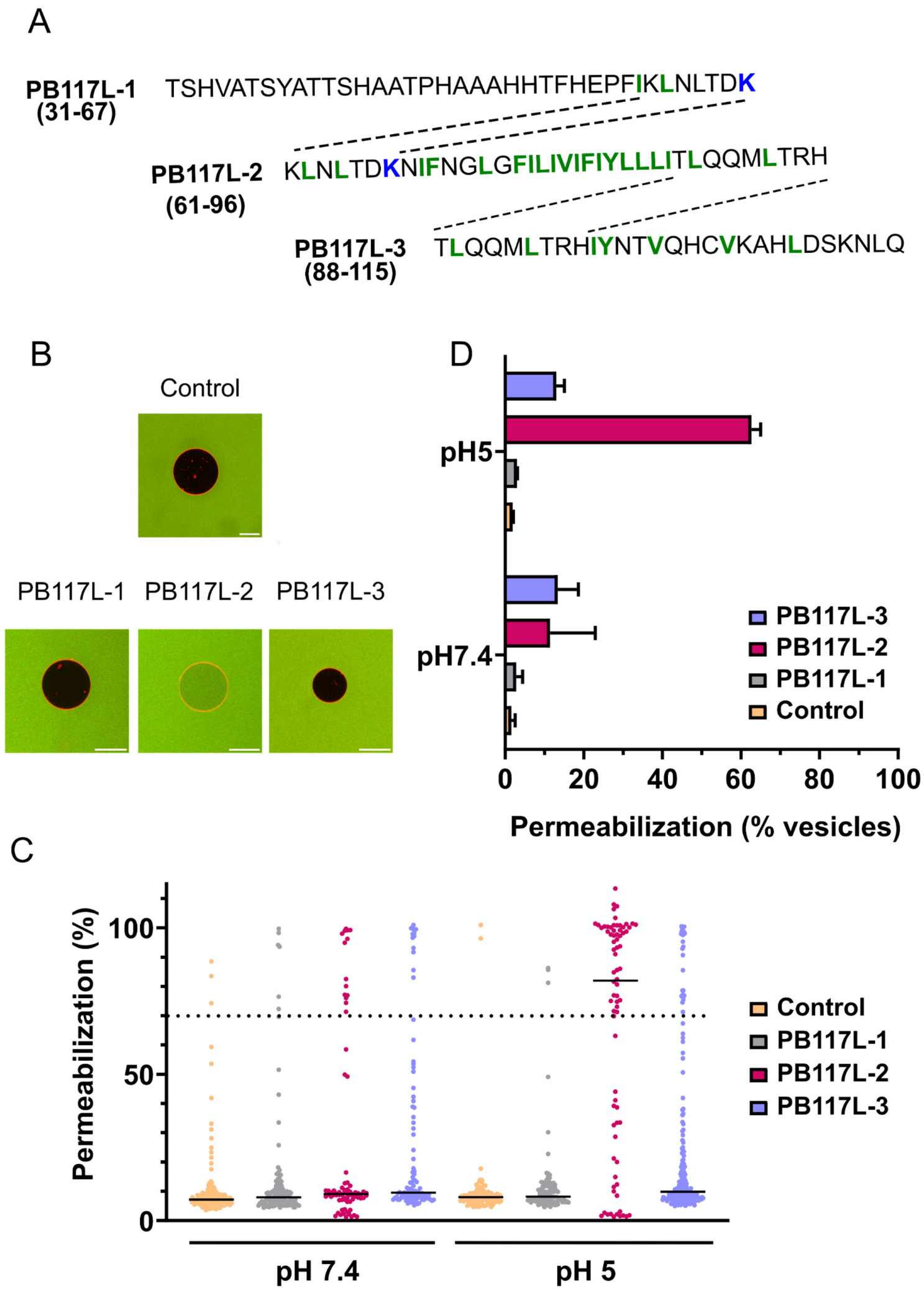
A
PB117L-1 (31-67) TSHVATSYATTSHAATPHAAAHHTFHEPFIKLNLTDK
PB117L-2 (61-96) KLNLTDKNIFNGLGFILIVIFIYLLLITLQQMLTRH
PB117L-3 (88-115) TLQQMLTRHIYNTVQHCVKAHLDSKNLQ
B
Control
PB117L-1
PB117L-2
PB117L-3
D
pH5
pH7.4
PB117L-3
PB117L-2
PB117L-1
Control
0
20
40
60
80
100
Permeabilization (% vesicles)
C
Permeabilization (%)
100
50
0
Control
PB117L-1
PB117L-2
PB117L-3
pH 7.4
pH 5

A

PB117L-2:
KLNLTDKNIFNGLGFILIV
IFIYLLLITLQQMLTRH

PB117L-2scr:
KLINLLIGFNVQYITGLLRFLILL
KQNDTMITHIF

B

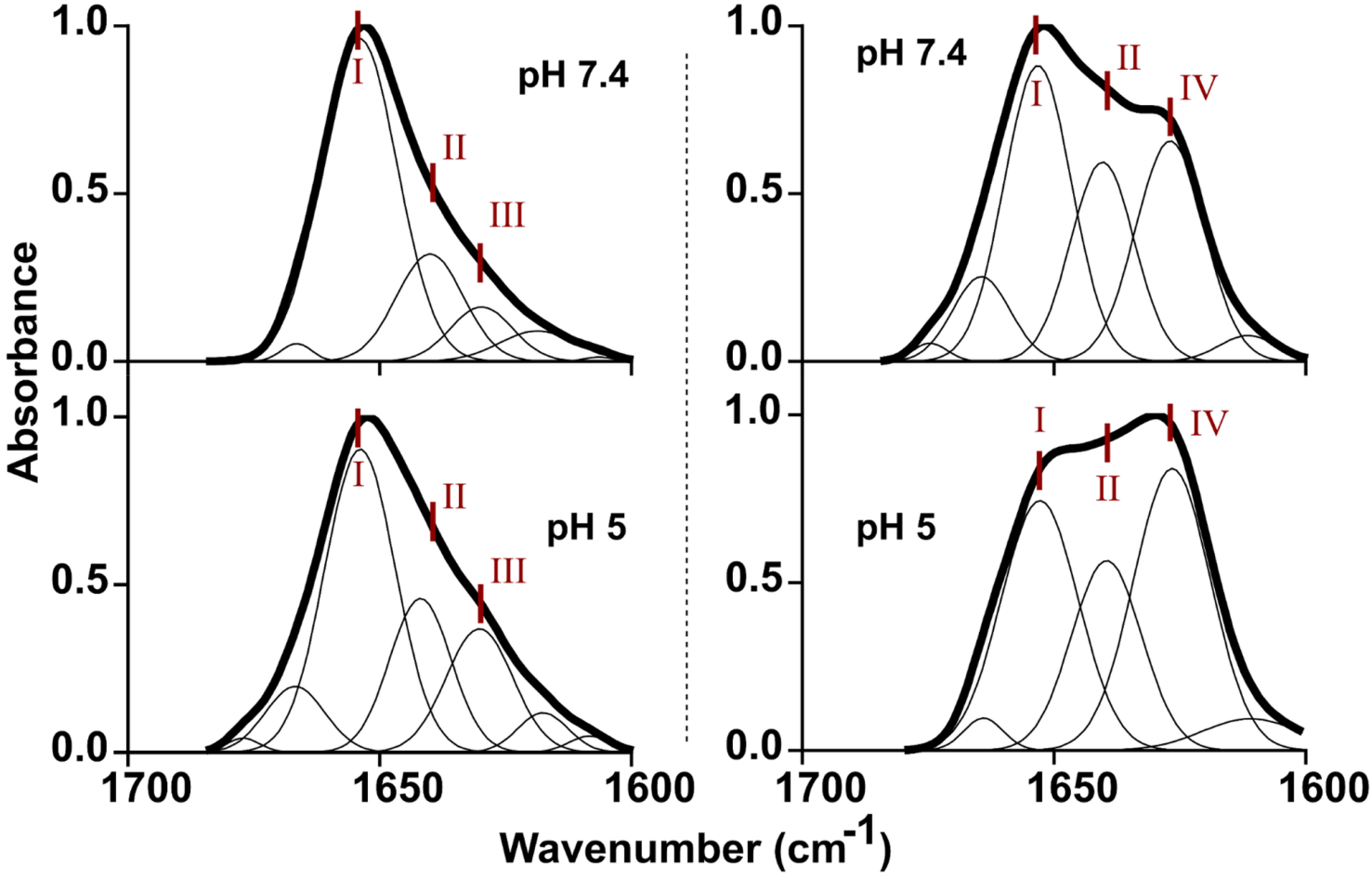

C